15182 Bolsa Chica Road, Suite D
Huntington Beach, CA 92649 USA

allied environmental technologies, inc.

COMPUTATIONAL FLUID DYNAMICS MODELING

APPLICATIONS FOR ENGINEERING SOLUTIONS

STATEMENT OF QUALIFICATIONS

Computational Fluid Dynamics for Engineering Solutions

ABSTRACT

Computational Fluid Dynamics (CFD) is becoming a critical part of the design process for more and more companies. CFD makes it possible to evaluate velocity, pressure, temperature, and species concentration of fluid flow throughout a solution domain, allowing the design to be optimized prior to the prototype phase.

At Allied Environmental Technologies, Inc. our philosophy embraces the idea that advanced Computational Fluid Dynamics (CFD) technology combined with an intelligent graphical interface results in a powerful simulation capability. Allied offers solutions to industry in aerodynamics, chemical, and combustion processes, environmental flows, and more. At the core of the CFD modeling is a three-dimensional flow solver that is powerful, efficient, and easily extended to custom engineering applications. We combined the Fluent's proven simulation capabilities in fluid flow, heat transfer, and combustion with years of practical experience in power and other industries.

In designing a new mixing device, injection grid or just a simple gas diverter or a distribution device, design engineers need to ensure adequate geometry, pressure loss, and residence time would be available. More importantly, to run the plant efficiently and economically, operators and plant engineers need to know and be able to set the optimum parameters. For example, to run the injection grid for cooling purposes, operator needs to know and be able to set the liquid flow through the orifices to achieve optimum droplet size to ensure a complete evaporation and proper mixing parameters. On the other hand, while running the same grid with the gaseous media injected, the operator needs to be concerned with the time required for achieve the proper mixing parameters only. For these cases, CFD tools are very useful.

In a multiphase flow model, equations for conservation of mass, momentum, and energy are solved for each phase (gas bubbles, solid particles and liquid). Additional equations are included to describe the interactions between the phases due to drag, turbulence and other forces. From the computed solutions, information on velocity, temperature, and concentration of each phase is available for the whole vessel. Other parameters, such as mixing time, gas hold-up and particle concentration, can be deduced from the computer solutions.

TABLE OF CONTENTS

EXECUTIVE SUMMARY

With the appearance of powerful and fast computers, new possibilities for replacing time-consuming model testing and field-testing have arisen. This involves solving the differential equations describing fluid motion, using either a finite volume or sometimes, but more rarely due to larger amount of CPU time required, a finite element method. These methods applied for the solution of the fluid equations of motion are named computation fluid dynamics or simply CFD.

CFD essentially takes the momentum, heat and mass balance equations, along with other models describing the equipment performance, and solves them to give information such as temperature profiles, velocity profiles and equipments size. The basic principle of the CFD modeling method is that the simulated flow region is divided into small cells within each of which the flow either kept under constant conditions or varies smoothly. Differential equations of momentum, energy, and mass balance are discretized and represented in terms of the variables at the center of or at any predetermined position within the cells. These equations are solved iteratively until the solution reaches the desired accuracy.

Flow Engineering

Allied Environmental Technologies, Inc. Flow Engineering offers a variety of services, which specifically support CFD model studies. We can conduct internal inspections to document areas of particulate buildup, wear patterns, and existing internal structural members, and flow devices. Filed airflow measurements within precipitators, scrubbers, SCR vessels, and flues could be conducted to evaluate flow problems prior to conducting a model study, or at the completion of a rebuild project to satisfy operational guarantees.

In addition to direct measurements and the CFD analyses, various methods of flow visualization could be employed. This visualization software helps to quickly understand the most complex features of ones simulation and effectively communicate ones conclusions.

CHAPTER 1. BACKGROUND

To gain acceptance and confidence in applying the CFD technology, numerous validation exercises were conducted in which CFD solutions were compared against measured values from experiments.

1.1 Computational Fluid Dynamics Modeling

Traditional restrictions in flow analysis and design limit the accuracy in solving and visualization fluid-flow problems. This applies to both single- and multi-phase flows, and is particularly true of problems that are three dimensional in nature and involve turbulence, chemical reactions, and/or heat and mass transfer. All these can be considered together in the application of Computational Fluid Dynamics, a powerful technique that can help to overcome many of the restrictions influencing traditional analysis.

The basic principle of the CFD modeling method is simple. The flow regime is divided into small cells within each of which the flow either kept constant or varies smoothly (the smooth variation is normally assumed for modern techniques that normally have order of accuracy above one). The differential equations of momentum, energy, and mass balance are discretized and represented in terms of the variables at the cell centers (collocated variables arrangement) or at a predetermined position within the cells (normally cell walls for velocities – staggered variable arrangement). These equations are solved until the solution reaches the desired accuracy.

CFD modeling provides a good description of flow field variables, velocities, temperatures, or a mass concentration anywhere in the region with details not usually available through physical modeling. It is especially useful for determining the parametric effects of a certain process variable. Once the basic model is established, parametric runs can usually be accomplished with reduced effort. In addition, CFD can be used to simulate some of the hard to duplicate experimental conditions or to investigate some of the hard to measure variables.

The compartment volume under study is divided into an array of small cells, and the equations of momentum, energy, and mass transfer are solved numerically within each cell. This provides a good description of flow field variables such as velocities, temperatures, and mass concentrations everywhere in the region. The boundary conditions for gas flow could be specified according to the thermodynamic, heat, and mass transfer characteristics at different gas flows and velocities. The mixing, distribution, and stratification could be then verified by inspecting the calculated pressure distribution across the exhaust duct.

The computational results, including the three-dimensional distribution of the flue gas velocity (flow) and the total pressure loss, are presented in both mathematical and graphical interpretation.

1.1.1 Fluid Mechanics.

1.1.1.1 Laminar and Turbulent Flows.

In fluid mechanics, it is customary and useful to classify fluid flow into several major categories, which for subsonic conditions usually are taken as ideal flow, laminar flow, and turbulent flow. Ideal flow refers to the flow of so-called ideal or frictionless fluids and is the type developed theoretically to a high state of mathematical perfection under the general designation of classical hydrodynamics. Although much criticized as a perfectionist and useless art, the results of this highly theoretical development have surprisingly wide range of practical applications in such broad fields as aerodynamics, wave motion, and supersonics. For example, even functioning of such commonplace devices as the Pitot tube depends on the theoretical results of classical hydrodynamics.

1.1.1.2 General Theory and Principal Equations.

Observations show that in any system involving fluid flow (either gas or liquid) two completely different types of this flow can exist. Reynolds first observed it in 1883 in his experiment in which water was discharged from a tank through a glass tube. A valve at the outlet could control the rate of flow, and a fine fragment of die injected at the entrance of the tube. At low velocities, it was found that the dye fragment remained intact throughout the length of the tube, showing that particles of water moved in parallel lines. This type of flow is known as *laminar*, viscous or streamline, the particles of fluid moving in an orderly manner and retaining the same relative positions in successive cross-sections.

As the velocity of the fluid was increased by the opening of the outlet valve, a point was eventually reached at which the dye fragment at first began to oscillate and then broke up. That resulted in a fact that the color was diffused over the whole cross-section. Thus, showing that the particles of fluid no longer moved in an orderly manner but occupied different relative positions in successive cross-sections. This type of flow is known as *turbulent* and is characterized by continuous small fluctuations in the magnitude and direction of the velocity of the particles, which are accompanied, by corresponding small fluctuations of pressure.

When the motion of a fluid particle an a stream is disturbed, its inertia will tend to carry it on the new direction, but the viscous forces due to surrounding fluid will tend to make it conform to the motion of the rest of the stream. In viscous flow, the viscous shear stresses are sufficient to eliminate the effects of any deviation, but in turbulent flow, they are inadequate. The criterion, which determines whether flow will be viscous or turbulent, is therefore the ratio of the internal force to the viscous force acting on a particle.

By dividing the characteristic inertia forces of the fluid flow to characteristic viscous forces of this flow, it is possible to find out that the ratio is proportional to dimensionless value

$$Re = \frac{\rho v l}{\mu}$$

where:

ρ is fluid density,
v is characteristic fluid velocity,
λ is characteristic length of the fluid flow and
μ is dynamic viscosity of the fluid.

This dimensionless value *Re* is known as Reynolds number. The value of the Reynolds number at which the flow ceases to be laminar and becomes turbulent depends on the flow geometry. However, usually the transition from laminar to turbulent flow occurs in the range 1,000-10,000 of the values of Reynolds number *Re*. Thus, to solve the problem accurately, we must provide the appropriate model that is able of handling the turbulent flows.

To obtain the stationary fields of velocity, pressure, and/or temperature for any fluid flow one has to solve the equations of motion of the fluid together with energy equation and equation of state of the fluid under appropriate boundary conditions. Theoretically, the equations of motion for both laminar and turbulent Newtonian flows are the same Navier-Stokes equations. However, in practice the solution of Navier-Stokes equations for the turbulent flow requires very small computational cell size due to necessity to accurately simulate small-scale turbulent eddies. This leads to very large computer memory consumption, which is possible only on modern-day supercomputers. Moreover, this kind of precision normally is not required for the engineering system where usually only time-averaged values of the flow are important and small turbulent velocity and pressure calculations are immaterial.

To avoid the unnecessary consumption of the computer time for the solution of the full-scale Navier-Stokes equations for the turbulent flow number of numerical techniques have been proposed. These are directed to determining the time-averaged values of the velocities and pressure in turbulent flows rather than instantaneous values of these parameters. The most popular for engineering problems among these techniques are so-called effective or turbulent viscosity techniques. The essence of effective viscosity techniques is that the viscosity used in the equations of motion of the fluid in the turbulent regime is not the real fluid viscosity (laminar viscosity), which does not depend on the parameters of the flow, but some effective viscosity which is determined according to the parameters of the turbulent flow and thus is no material constant and which is usually larger than the laminar viscosity. The introduction of this effective viscosity allows us to determine the field of the mean turbulent parameters of the flow in similar way as it is done for the parameters of the laminar flow. While the effective viscosity techniques are not perfect and sometimes produce wrong solutions, they have been around for several decades already and all their shortcomings are well documented in the literature. At the present day, the effective viscosity techniques are perhaps the only techniques used for the solution of the engineering problems, which involve flow of the fluids in the turbulent regimes.

One of the most popular effective viscosity models for the simulations of turbulent flow historically was the standard high Reynolds number Harlow-Nakayama k-ε model of the turbulent flow incorporated into the CFD software package has been used. The model provides the time-averaged values of velocities and pressure of the air throughout the system. This model has become perhaps the most popular two-equation model of turbulence, though mostly for historical rather than scientific reasons. K-ε model calculates the effective viscosity associated with the turbulence based on the solution of two equations for the density of turbulent kinetic energy k and rate of the dissipation of this energy ε. Since two additional differential equation have to be solved in this model, it belongs to the class of two-equation turbulence models. Like other two-equation models, the k-ε model is free from the need to prescribe the length scale distribution.

1.1.1.3 Boundary Conditions

In many reaction systems, determining the boundary conditions is more difficult than performing the time-dependent simulation. It is not very meaningful to calculate a time-dependent event in a system if one does not know how the initial state ha occurred, even if the initial state is known. Calculating a time-dependent event always must start from a stationary state.

The high-Reynolds number k-ε model becomes invalid near the walls and thus has to be regarded with the set of wall functions (low-Reynolds number models are also available but rarely used in engineering community). Allied Environmental Technologies, Inc. uses the approach of the logarithmic wall functions based on the ideas of Schlichting. These functions are applicable for the Reynolds numbers based on the length of the system, which are in the range from approximately 10^6 to 10^9. The structure of these functions depends strongly on the roughness of the walls since the increased roughness actually promotes development of the turbulence in the boundary layer and thus changes flow characteristics. In addition, even in the places where turbulent flow is fully developed the characteristic size of the wall roughness could be bigger that the thickness of this boundary layer. In this case, the flow will be greatly influenced by the wall roughness. Unfortunately, for the most cases the actual value of the wall roughness is not known. In cases like that, where the actual value of the wall roughness is not known it has been standard CFD practice to ignore the wall roughness at all and to assume the walls of the system to be smooth ones. In our simulation, we followed this standard practice for unknown roughness wall boundary conditions.

The other boundary conditions applied are fixed mass flow rate at the exit of the system and fixed static pressure at the entrance to the system. The inlet boundary conditions require the prescription of the two turbulent parameters, density of the kinetic energy of turbulence k and rate of the dissipation of this energy ε. These values are unknown, however they can be determined if we assume the intensity of the turbulence at the entrance. This allows us to determine the value of k, the value of ε is than determined based on the inlet linear dimensions. The inlet turbulence intensity is normally assumed to be between 1% and 5%, 2% value has been chosen for our calculations.

The equation of state of air was assumed the one of the constant density gas. This assumption is valid since the static pressure drop through the system is of order of several inches of water. This value is less than 1% of the atmospheric pressure, and the expected density change is less than one percent. Braden Manufacturing has provided the flow rate in the Filter House. The entrance conditions of the air were assumed the standard ones.

CHAPTER 2. REFERENCES

Following is an abbreviated list of our customers:

1. Braden Manufacturing, LLC
2. GE Power Systems
3. Lurgi GmbH and Lurgi, Inc.
4. TurboSonic, Inc.
5. AES, Inc.
6. Savage Zinc, Inc.
7. Deltak
8. GEA, Inc.
9. Nanticoke Generating Station, Ontario Power
10. Mirant, Inc.

CHAPTER 3. CASE STUDIES

3.1 FILTER HOUSE.

3.1.1 Model Setup.

The Filter House configuration includes four filter units placed in arrow formations with each unit containing a pre-filter, a filter, and a mist eliminator. In the present simulation, as in the previous one, the special care has been taken to include fine structural details in the simulation. These details include filter housing hood, details of the filter and pre-filter grid, cooler tanks, support columns, half-pipe situated at the top of the filter housing exit and vertical-horizontal braces according to the drawings provided by the customer.

The computational mesh has been constructed using the specifications provided by the customer using the body-fitted coordinates approach, which allows the creation of the grid of complex geometry. The computational grid consisted of 52 x 32 x 28 or 46,592 computational cells. The Figures below depict the structure of the computational cells for the simulations considered. In fact, only one half of the Filter House ductwork has been actually simulated, which was made possible by a complete symmetry with respect to the vertical plane passing through the center of the Filter House.

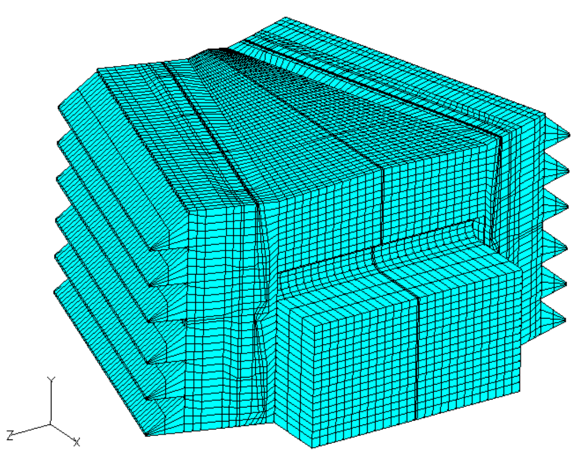

Computational Grid. View 1.

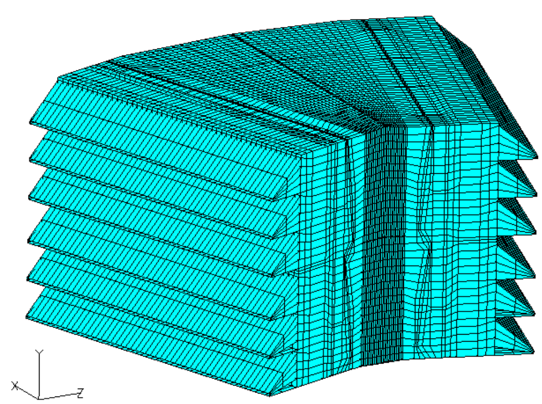

Computational Grid. View 2.

3.1.2 Results Discussion.

A number of cases had been evaluated. In the present simulation, complicated patterns of perforated screens with variable permeability were installed in the Plane A (downstream of evaporative cooler modules). The whole length of the cooler modules was divided into four parts (Zones); each Zone being 8.5 feet long.

- Zone 1 – (closest to the exit from the module) contains screens with 20%, 25% and 45% open space;
- Zone 2 – contains screens with 20%, 30% and 45% open space;
- Zone 3 – is covered by the screens with 45% open space, and
- Zone 4 - the last part, has no screens at all.

The computational results, including the three-dimensional distribution of the flue gas velocity (flow) are presented graphically below. The maximum velocity in the Plane A was computed to be 832 ft/min, while the total pressure loss across the filter house is 2.19 inches of water.

Furthermore, the results of the gas velocity calculated for all cases in the selected plane C are presented in a form of Contour Lines. There are six contour lines (where appropriate values are reached) colored from blue to red. These lines correspond to values:

- #1 – 500 ft/min
- #2 – 600 ft/min
- #3 – 700 ft/min
- #4 – 800 ft/min
- #5 – 900 ft/min
- #6 – 1000 ft/min.

3.1.3 Figures.

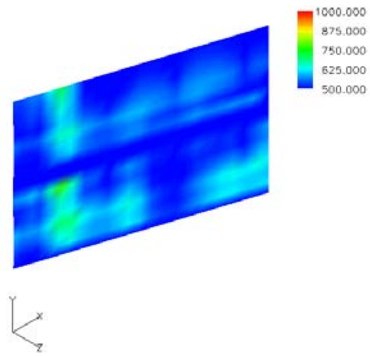

Plane A velocity values (ft/min).

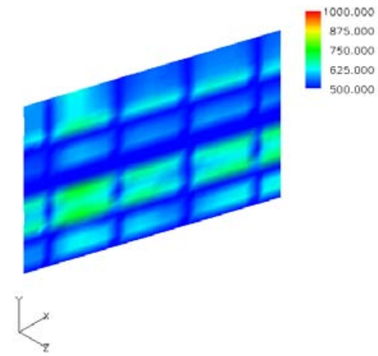

Plane B velocity values (ft/min)

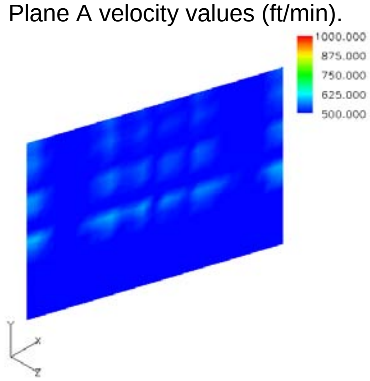

Plane C velocity values (ft/min).

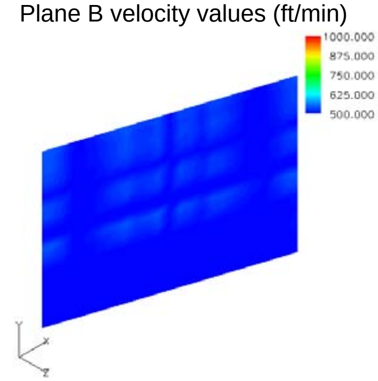

Plane D velocity values (ft/min).

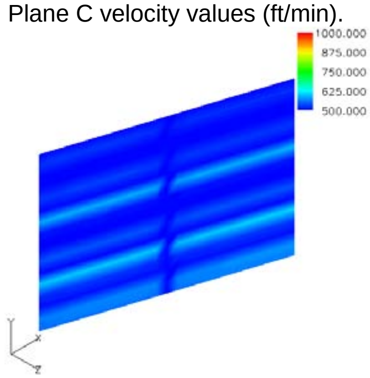

Plane E velocity values (ft/min).

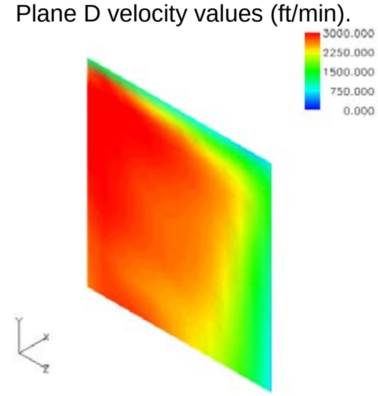

Plane F velocity values (ft/min).

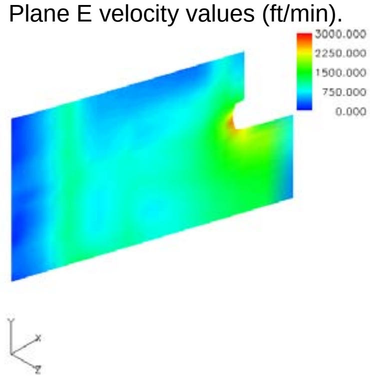

Plane G velocity values (ft/min).

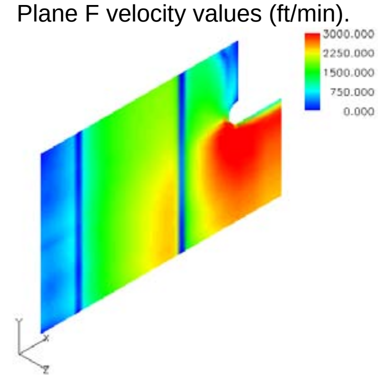

Plane H velocity values (ft/min).

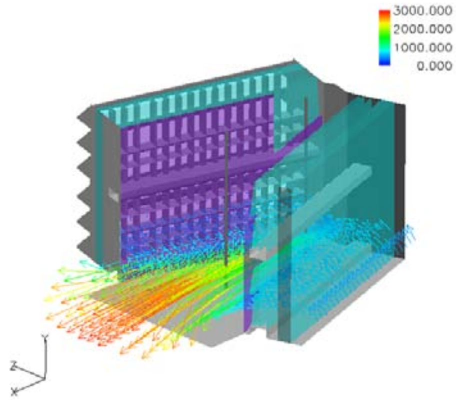

Velocity distribution in the horizontal plane situated at 1/12 height of the filter housing from the bottom of the modules.

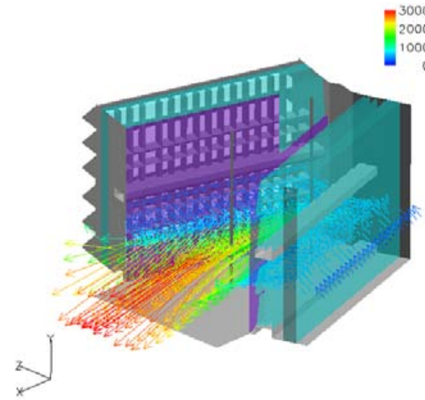

Velocity distribution in the horizontal plane situated at 1/4 height of the filter housing from the bottom of the modules.

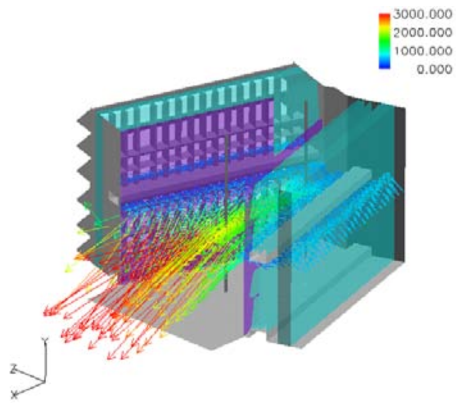

Velocity distribution in the horizontal plane situated at 5/12 height of the filter housing from the bottom of the modules

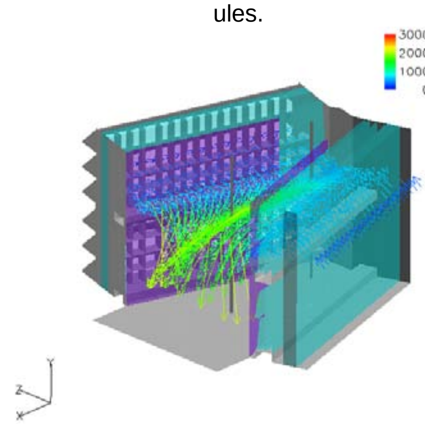

Velocity distribution in the horizontal plane situated at 7/12 height of the filter housing from the bottom of the modules.

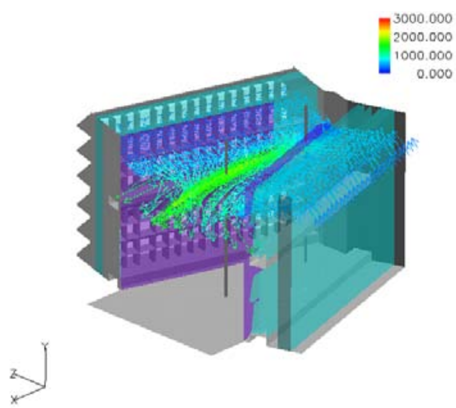

Velocity distribution in the horizontal plane situated at 9/12 height of the filter housing from the bottom of the modules.

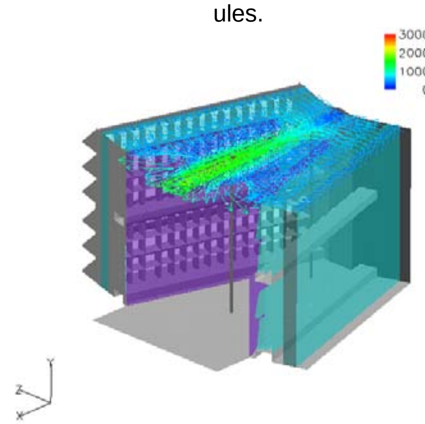

Velocity distribution in the horizontal plane situated at 11/12 height of the filter housing from the bottom of the modules

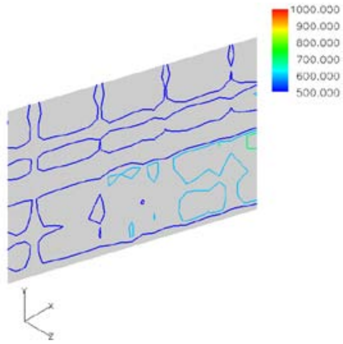

Case 1. Plane C Velocity contour lines (ft/min).

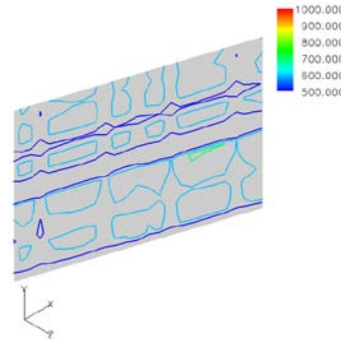

Case 2. Plane C Velocity contour lines (ft/min).

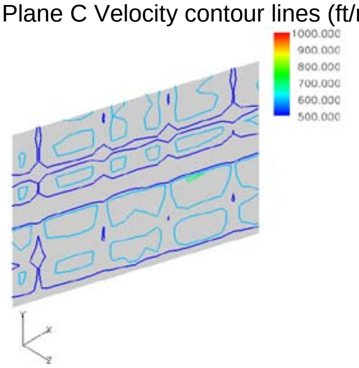

Case 3. Plane C Velocity contour lines (ft/min).

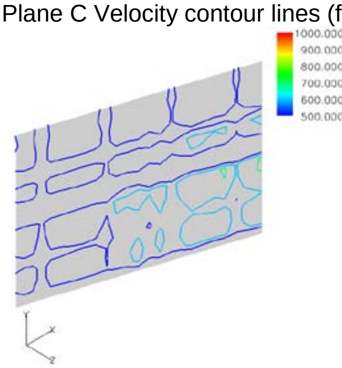

Case 4. Plane C Velocity contour lines (ft/min).

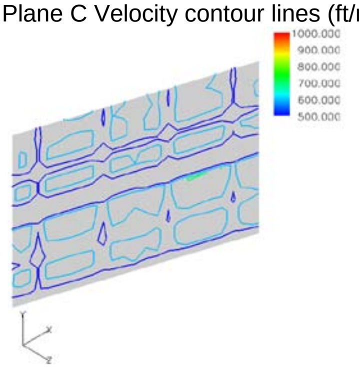

Case 5. Plane C Velocity contour lines (ft/min).

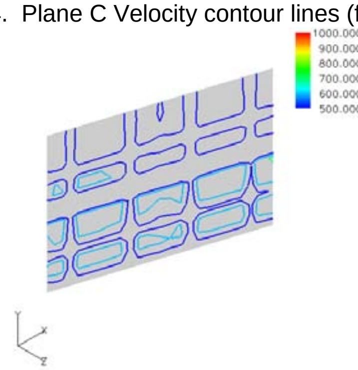

Case 6. Plane C Velocity contour lines (ft/min).

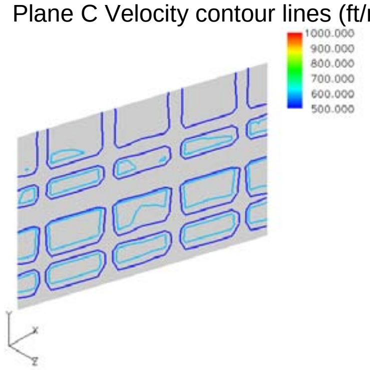

Case 7. Plane C Velocity contour lines (ft/min).

3.2 Combustion Gas Turbine Exhaust System

3.2.1 Geometry and Boundary Conditions

A computational domain for the gas turbine exhaust system is shown in Figure 1 below at different viewing angles. The blue region is the inlet where the exhaust gas from the gas turbine enters the diffuser duct. The diameter at the inlet is 4.877 m (16'). The inlet is then connected with a diffuser duct that gradually transforms the circular duct to a rectangular duct of larger cross-sectional area. In the rectangular section, nine identical silencer plates are visible on the plot. The panels have a length of 6.045 meters (19' 10"). At the upstream direction, there is a half cylinder of 0.254-meter (10") radius. The width of all the panels is 0.508 m (20"). The gap between the panels is 0.305 m (12"). The gap between the outmost panel and the external wall is 0.152 m (6").

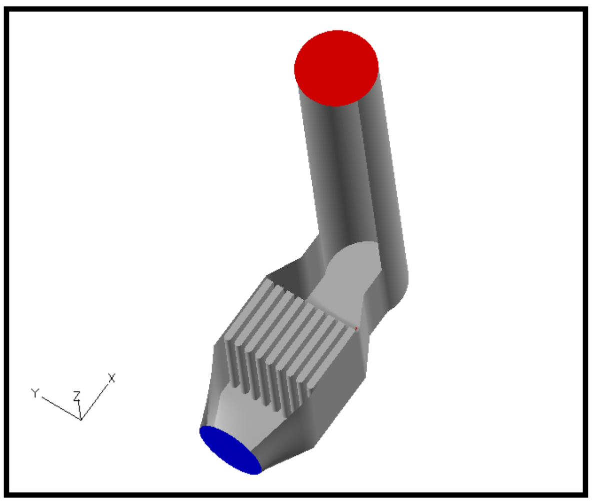

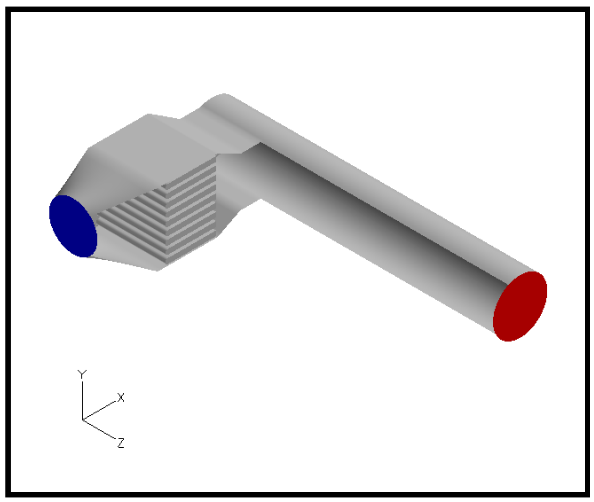

Figure 1. Cut-off view of the computational domain. The blue region is the inlet where the exhaust gas from the gas turbine enters the diffuser duct. The silencer plates are visible. At top of the stack, the outlet is represented with a red region

The entire computational domain was divided into a number of structured cells. The dimension of the mesh is 43x72x56. The total number of cells is 173,376.

The exhaust gas has a temperature of 890.5°K (1143.5°F). The pressure is 99632.75 N/m^2 (14.45 psia). The molecular weight of the gas is 28.10, and the density is 0.378 kg/m^3. The viscosity of the gas is set to be 39.227x10^{-6} N sec/m^2. The incoming gas flow rate is 892.9 Lb/sec (405.86 kg/sec), which corresponds to an average incoming velocity of 6.1046 m/sec at inlet. The exhaust gas from the last stage GT bucket has a swirl angle of 4.22 degrees.

Two cases were considered for the inlet velocity profile. For the uniform inlet case, a constant incoming u (x-direction) velocity component was specified. While the v (y-direction) and w (z-direction) according to the swirling angle. Whereas, for the non-uniform inlet case, u velocity values at the following four locations are specified:

	R/R_0=0.00	R/R_0=0.38	R/R_0=0.70	R/R_0=1.00
U/V_{ave}	0.55	1.09	1.37	0.10

The Lagrange Interpolation formula was used to determine the u velocity at other radial positions. After the u velocity is calculated, the v and w velocity is determined according to the swirling angle.

Though the ambient temperature is 95°F, the computational domain is wrapped with insulation and the calculation is done with adiabatic no-slip boundary condition for all internal surfaces. Furthermore, the walls are assumed to be smooth. The pressure variation within the domain is relatively small compared to the ambient pressure. Thus, the fluid is approximated with incompressible fluid with the properties as specified above.

The k-e two-equation turbulence model is applied to simulate the turbulent flow. The incoming gas was assumed to have 1% free stream turbulence kinetic energy. The dissipation rate is determined by using the above turbulence kinetic energy with the inlet diameter (4.877 m) as the characteristic length scale. Unless known quantities are measured at the inlet for the turbulence properties, this is a common practice for k-e treatment at inlet and has been applied for many turbulent flow simulations. The standard wall function treatment is adopted for all non-slip walls.

3.2.2 Results and Discussion for Uniform Inlet

Figure 2 below present three-dimensional cutoff views of the geometry with two perpendicular cut planes showing the flow patterns.

The friction effects from the no-slip walls and the diverging diffuser duct geometry lead to non-uniformity of velocity at the edges. However, the velocity at the center portion is virtually uniform. The effects of the silencer panels can be seem from the plots below. The graph on the left reveals that the center channels have higher velocity magnitude. Furthermore, the high velocity region shifted toward higher elevation (+Z direction). It is because the flow is about to turn upwards in the vertical stack. It is also because the bottom wall inclines upwards behind the silencer panels.

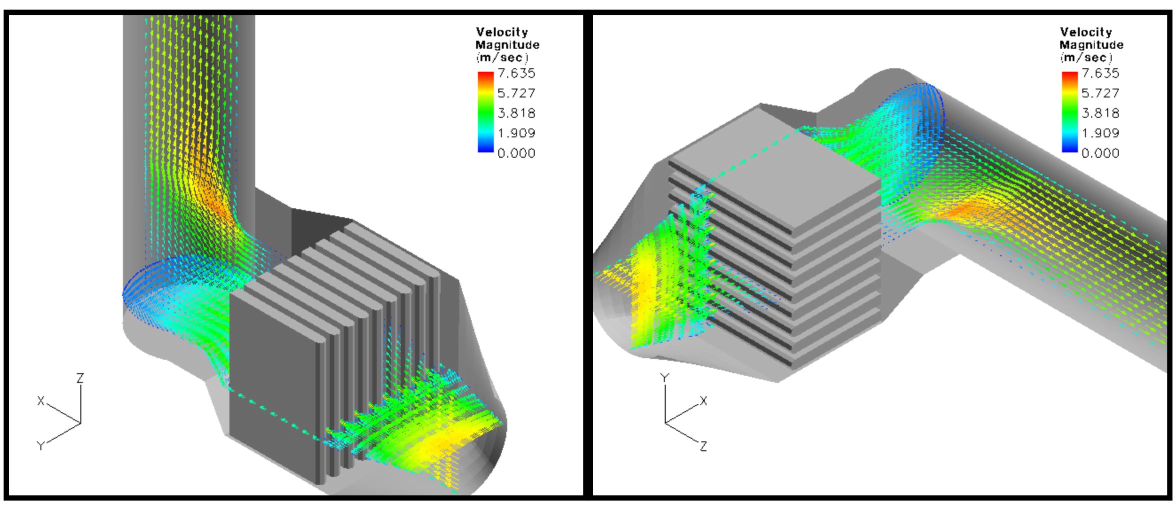

Figure 2. The cutoff view of the exterior walls with the silencer panels. There are two cut planes of velocity vectors showing the velocity vectors through the center symmetric plan and horizontal velocity vectors. The colors of the vectors indicate the magnitude of the velocity.

Within each flow channel, the flow shows similar pattern that has higher center velocity. It is characteristics for flow between parallel plates.

The 3-D effects are obvious on the plots. The following Figure 3 depicts the top view of a cut plane of flow through the centerline of the inlet (Z=0). The incoming uniform flow expands as it enters diffuser duct. The existence of the silencer panels reduces the area available to the flow. Thus, the velocity magnitude in the center of the channels speeds up. The center channels have higher averaged velocity than the outside channels. This confirms the same observation from the previous Figures.

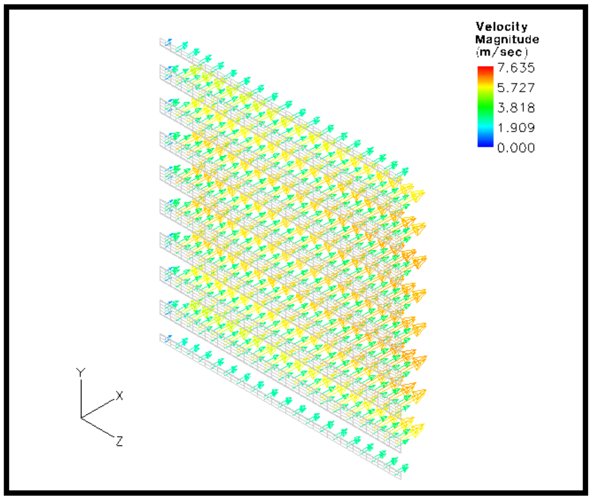

Figure 3. This is the velocity distribution at the end of the silencer panels. The upper portion (+Z-direction) has higher velocity than those at lower portion.

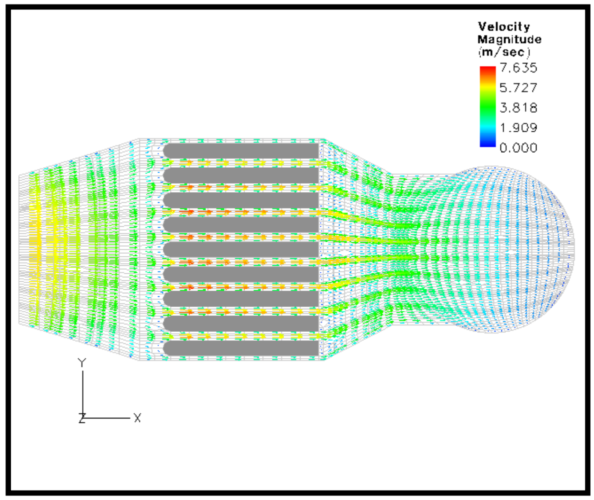

Figure 4. This is the top view of a cut plane of flow through the centerline of the inlet. The incoming uniform flow expands as it enters diffuser duct. The existence of the silencer panels reduces the area available to the flow. Thus, the velocity magnitude in the center of the channels increases. The center channels have higher averaged velocity than the outside channels. The jets exiting from the channels are also obvious in this plot.

3.2.3 Results and Discussion for Non-Uniform Inlet

The Figure 5 presents three-dimensional cutoff views of the geometry with two perpendicular cut planes showing the flow patterns.

The Figure 6 is a horizontal plane cuts through the centerline of the inlet. This is the Z1-Z1 plane similar to the one before. The Figure 7 depicts the top view of a cut plane of flow through the centerline of the inlet (Z=0). The incoming flow distribution is quite visible. After entering the diffuser duct, it expands horizontally (Y-direction) as well as vertically. The existence of the silencer panels reduces the area available to the flow. Thus, the center channels have higher averaged velocity than the outside channels. However, the distribution of flow in all channels is more even than case with the “uniform” inlet.

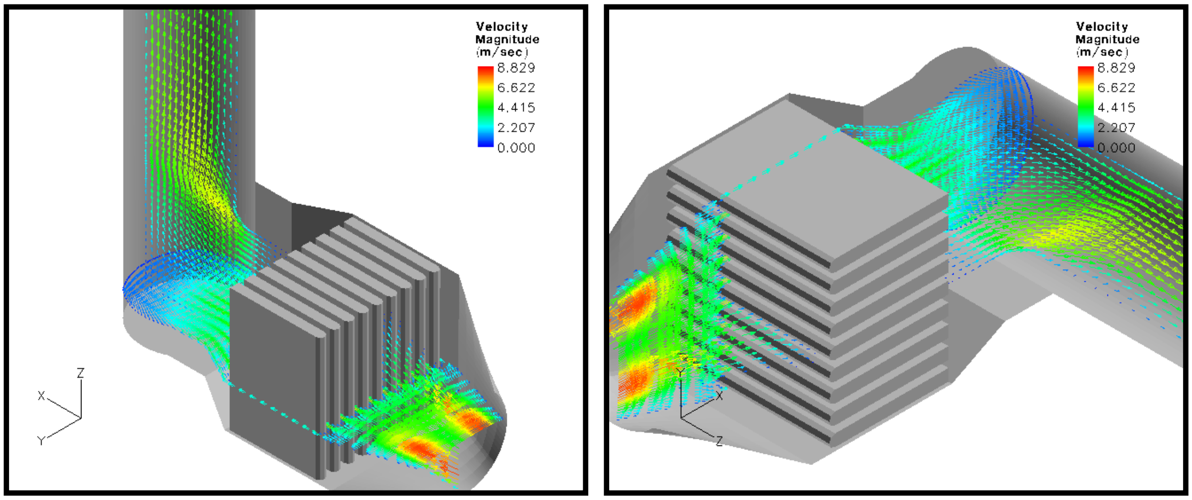

Figure 5. The cutoff view of the exterior walls with the silencer panels. There are two cut planes of velocity vectors showing the velocity vectors through the center symmetric plan and horizontal velocity vectors. The colors of the vectors indicate the magnitude of the velocity. The non-uniformity of inlet velocity can be seen.

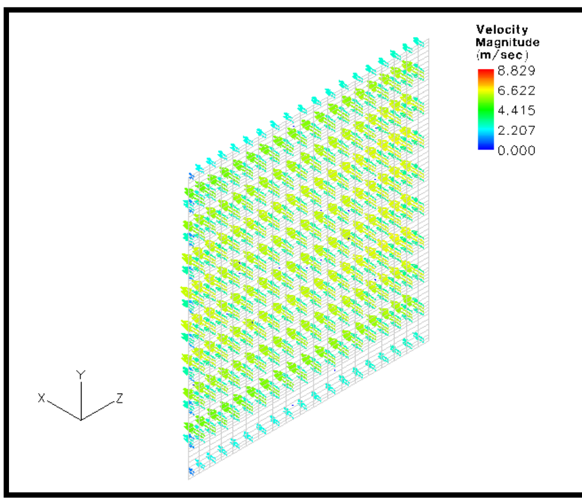

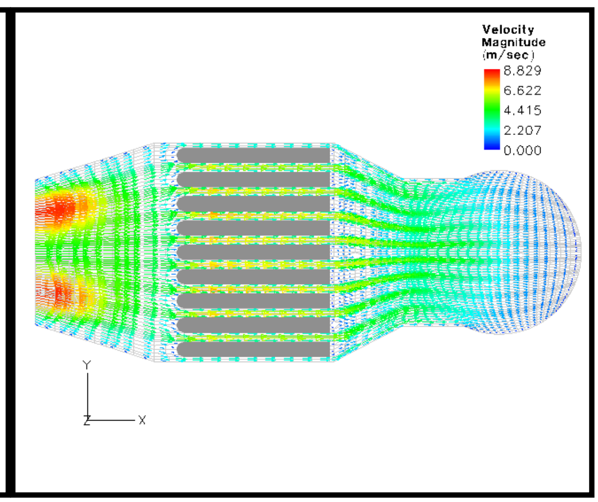

Figure 6. This is the velocity distribution at the end of the silencer panels. It could be seen that the upper portion (+Z-direction) has higher velocity than those at lower portion.

Figure 7. The Figure above depicts the top view of a cut plane of flow through the centerline of the inlet. The incoming non-uniform flow expands as it enters diffuser duct. The existence of the silencer panels reduces the area available to the flow. Thus, the velocity magnitude in the center of the channels speeds up. The averaged velocity distribution in the channels seems more uniform the other case that has uniform inlet velocity. The reason is probably due to the rela-

tively higher inlet flow nears the wall compensates the wall friction. The jets exiting from the channels are also obvious in this plot.

The next two figures present the vertical plane cut for the "uniform" (left) and the "non-uniform" (right) cases respectively. The non-uniform inlet flow distribution could be easily seen on the Figure 8.

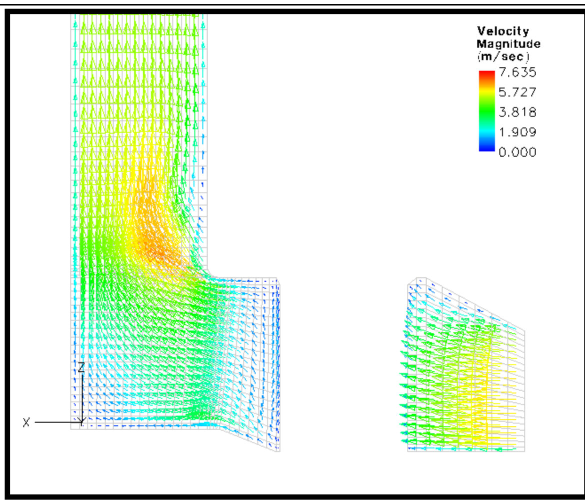

Figure 8. A vertical cut plane cutting through the center of the model (Y = 0.0 m). Geometrically, this is the symmetric plane. However, due to the swirling, this is not a symmetric plane of the flow. Since this cuts through a silencer panel, there is no flow in the silencer region. The expansion of the flow at diffuser can be seen on the left of the plot. The flow turn from horizontal direction to vertical stack is also shown.

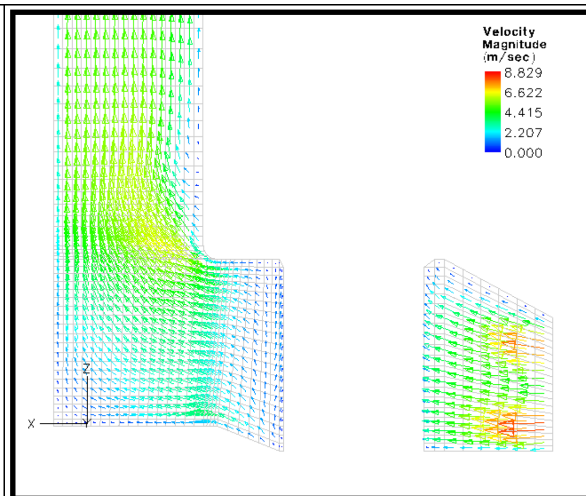

Figure 9. A vertical cut plane cutting through the center of the model (Y = 0.0 m). Geometrically, this is the symmetric plane. However, due to the swirling, this is not a symmetric plane of the flow. Since this cuts through a silencer panel, there is no flow in the silencer region. The expansion of the flow at diffuser can be seen on the left of the plot. The turning of flow from horizontal direction to vertical stack is shown in this plot.

Overall, the averaged pressure difference between the inlet and outlet for case 2(non-uniform inlet) is 809 N/m^2 or 3.25 inches of water, while the total pressure loss for this case is 816 N/m^2 (or 3.27 inches of water).

3.2.4 Conclusions

- The uniform and non-uniform gas exhaust flows were simulated for the Exhaust Ductwork System. In both cases, the flow reached fully developed profile in the vertical stack. The flow in those regions is uniform in the center of the stack with a thin boundary layer. Design of the connecting bend between the horizontal housing and the vertical bend allows the flow to turn from horizontal direction to vertical direction without separation. Though there is secondary flow caused by the turning, it reaches fully developed before exit.

- The silencer panels force the fluid to flow between the parallel walls. However, the fluid is still allowed to shift upwards as the downstream stack influences it.
- The silencers cause the fluid to form jets exiting the channels. The panels also induce small recalculation region right behind each panel.
- Flow distribution among the channels in the silencer region has similar characteristics for both cases. However, the distribution is more even for the non-uniform inlet case.
- The average pressure drop for both cases is quite similar. For the uniform gas flow at the inlet, the average pressure drop is 3.12 inches of water. Whereas, for the Case 2, non-uniform inlet, the average pressure drop is 3.25 inches of water.

The total pressure drop is 3.13 and 3.27 inches of water for both cases respectively.

3.3 Hot Gas Precipitator

The entire region of the simulation consisted of the three-dimensional model of the hot gas electrostatic precipitator. The computational results, including the three-dimensional distribution of the flue gas velocity (flow) are presented graphically on the figures below.

The hot gas electrostatic precipitator design considered includes addition of the "variable aperture" gas distribution device at the precipitator inlet. The purpose of this device is to create a controlled non-uniform gas distribution at the inlet to direct more airflow upwards, thus creating lower gas velocities at the bottom portion of the precipitator. This device is presented by a grid of vertical channels, which are situated to allow for larger gas flow at the top and lower towards the bottom. The geometry also includes gas distribution grid at the exit from the electrostatic precipitator and set of baffles and internal walkways.

The inlet grid had been tuned to allow for open areas of 60% and 40% at the top and the bottom respectively with the gradual convergence in between.

It has been shown that the addition of the "variable flow" type gas distribution device at the precipitator inlet does improve the gas flow distribution.

3.3.1 Gas Flow in Electrostatic Precipitators

Gas flow is fundamental to electrostatic precipitation. Its influence on overall performance is equal to or greater than of the corona and the electrostatic forces acting on the particles. Type of gas flow determines the character of particle collection, leading to a deterministic algebraic law for laminar flow and to a probability exponential law for turbulent flow. Disturbed gas flow, in the form of excessive turbulence, gas jets, swirls, pulsations, and other unbalanced erratic flow conditions, in general causes heavy reentrainment loss from electrodes and hoppers, as well as poor collection initially. Evidence from countless case histories shows the magnitude of these effects on precipitator performance. It is common experience to increase precipitator efficiency simply by correction and improvements in gas flow.

Despite the importance of gas flow and the serious, often disastrous, effects of mal-flow on precipitators operation, scientific investigations of gas flow phenomena and problems in this field date only from about 1945.

Application of fluid mechanics principles to industrial gas flow band to electrical precipitation has followed a sporadic, rather than a smooth, scientific path. Adaptation of results and theories from the relatively sophisticated filed of modern aerodynamics has been difficult because of fundamental differences in conditions and the primitive state of industrial gas-flow technology[1]. Actually, the philosophy and methods followed have been more akin to the semi-empirical hydraulics of the nineteen-century than to aerodynamics, with the exception of qualitative use of Prandtl's boundary-layer concept and Taylor's statistical theories of turbulence.

3.3.1.1 IGCI EP-7 Standard

The US "International Gas Cleaning institute" (IGCI) published EP-7 in November 1970. It deals with "standards" for gas distribution and model testing[3]. In this publication, it is clearly pointed out that the gas distribution demands are subordinate to the emission guarantee and need not be corrected, if it does not comply with IGCI EP-7, as long as the emission guarantee is met.

IGCI EP-7 lays down requirements as to a number of measuring points, their distribution and the subsequent evaluation and statistics, e.g. it demands that 85% of the velocities in a cross-section, 3 feet (0.9.m) downstream of the leading edge of the first filed, are less than or equal to 1.15 times the average velocity. Furthermore, 99% must be less than or equal to 1.40 time average. The same need apply to a cross-section 3 feet (0.9 m) from the outlet of the last field. Specific demands with 1.10 instead of 1.15, and 90% instead of 85% are not motivated by precipitator physics, but merely in an attempt to demonstrate effective project management.

In the case of a presumed normal velocity distribution the [1.15|85%] claim corresponds to a certain coefficient variation, $\frac{\sigma}{v_m}$, σ being the standard deviation and υ_m the mean velocity.

Experience seems to indicate that σ is almost independent of mean velocity. In fact, the lower the average velocity, the more difficult it will be to obtain a good gas distribution, and $\frac{\sigma}{v_m}$ increases with decreasing mean velocity.

3.3.2 Electrostatic Precipitators

The hot gas precipitators were supplied by Wheelabrator-Frye, Inc. based on Lurgi design. The precipitators were designed with a single chamber each having individual inlet and outlet nozzles.

The precipitator has two mechanical and electrical fields in the direction of the gas flow. Each field is 14 feet 1⅛ inches long by the 22 feet effective collecting plates' height. There are 17 gas passages on 12 inch spacing in each chamber. A common dust-collecting hopper is serving both fields.

The case study included two gas distribution grids, one at the precipitator inlet and the other at the precipitator exit. The exit grid consists of 14 vertical channels positioned with the constant width. The inlet grid, on the other hand, although also consisting of 14 vertical channels has those tapered so that the open area of the grid is gradually converging from 60% and 40% top to bottom respectively.

At the design operating gas flow of 54,010 acfm, the precipitators have a specific collecting area (SCA) of 388 ft^2/1,000 acfm. Precipitator design and operating details are described in the Table below.

NO.	UNIT ID == >			Unit 1			
	Case ID ===>			Design Data		Oper./Calc. Data	
	FGC Option === >						
	ITEM			English	Metric	English	Metric
1	Standard	Temperature	Deg. F. - Deg. C	32	0	32	0
2	Conditions	Pressure	Hg - mm. H2O	29.92	760	29.92	760
3	Design Inlet Conditions	Temperature	Deg. F - C	660	349	660	349
4		Moisture	%				
5		Site Elevation	ft - m	500	152	500	152
6		Design Heat Input	MBtu/hr				
7		Coal Heat Value	Btu/lb				
8		Fuel Burn Rate	lb/hr				
9		Gas Volume/100 lb coal	scf, dry				
10		Flue Gas Flow, dry	cfm - Nm3/s				
11		Flue Gas Flow, wet	cfm - Nm3/s				
12		Flue Gas Flow, actual	acfm - m3/s	54,010	25	54,010	25
13		Fly					
14		Ash					
15		Concentration	gr./acf - g/m3	3.560	8.149	3.560	8.149
16		Loading	lb/MBtu				
17	General ESP Data	ESP/Blr	No.	1	1	1	1
18		Chambers/ESP	No.	1	1	1	1
19		Cells/CH	No.	1	1	1	1
20		Gas Passages/Cell	No.	17	17	17	17
21	Collecting Electrodes	Spacing (Plate-to-Plate)	in - mm	12	305	12	305
22		Field 1	ft. - m	14.00	4.27	14.00	4.27
23		Field 2	ft. - m	14.00	4.27	14.00	4.27
24		Height	ft. - m	22.00	6.71	22.00	6.71
25	Design Details	Coll. Area/Precip.	sq. ft. - m2	20,944	1,946	20,944	1,946
26		Total ESP El. Length	ft. - m	28.00	8.53	28.00	8.53
27		Total Collecting Area	sq. ft. - m2	20,944	1,946	20,944	1,946
28	Calculated Values	SCA	sq. ft./k acfm - m2/m3/s	387.78	76.33	387.78	76.33
29		Aspect Ratio		1.27	1.27	1.27	1.27
30		Face Velocity	ft./s - m/s	2.41	0.73	2.41	0.73
31		Treatment Time	s	11.63	11.63	11.63	11.63
32	Efficiency Data	Migration Velocity (D/A),cm./s	cm./s	5.12	5.13	5.12	5.13
33		Modified migration vel., (k=.5)	cm./s	20.05	20.05	20.05	20.05
34		Estimated Eff.	%	98.00	98.00	98.00	98.00
35	Outlet Conditions	Fly Ash	gr./scf - mg/Nm3, wet				
36		Concentration	gr./acf - mg/m3	0.0712	162.98	0.0712	162.98
37		Mass Emissions	lb/MBtu				
38	Stack Opacity	Exit Stack Dia.	ft. - m				
39		Computer Estimated	%				

3.3.3 Model Setup.

The computational mesh has been constructed using the specifications provided by the customer utilizing the body-fitted coordinates approach, which allows the creation of the grid of complex geometry. The structure of the computational cells (computational mesh) is depicted on Figures 1 and 2 below. Only one half of the total electrostatic precipitator ductwork has been actually simulated, this is possible due to symmetry with respect to the vertical plane passing through the center of the electrostatic precipitator. The computational grid consisted of 81 x 65 x 18 or 94,770 computational cells. The distinct parts of the computation are depicted in Figure 3, which shows the position of the internal details in the hot gas electrostatic precipitator CFD model.

The flow velocity vectors are depicted in the central vertical section of the electrostatic precipitator (Figure 5). These were also computed in the sections (planes) of the precipitator shown on the Figure 4. The results are represented by Figures 6 through 13. The last two figures (Figure 12 and Figure 13) show the distribution of the gas flow in the planes where parameters of this distribution were calculated. These planes are numbered 7 and 8 on Figure 4.

3.3.4 Results Discussion.

This study represents results of the CFD simulation of the hot gas precipitator with an additional gas distribution device installed at the precipitator inlet. The latter is of “variable aperture” or tapered design, for it has 60% open area at the top gradually converging to 40% open area at the bottom. The purpose of this grid is to redistribute the gas flow in the precipitator upward to assure lower gas velocities at the bottom in the hopper area to further improve overall precipitator collection efficiency.

Analyzing velocity vectors on Figures 5 through 13, it could be see that number of vortices is being formed inside the hot gas electrostatic precipitator. The flow of the gas is entering the system from the above, and, as a result, has a rather significant downward component present throughout the electrostatic precipitator. While the horizontal guiding vanes at the entrance of the electrostatic precipitator redistribute this flow to a certain degree, they are unable to eliminate this downward flow. Big portion of the flow is directed downward to the hopper section, this flow hits the hopper baffle and starts to recirculate. The recirculation leads to high velocities of the gas flow near the precipitator front with respect to the flow direction wall of the hopper, these large velocities could be seen on Figures 5 – 6 and 9. Even the presence of the "variable aperture" gas distribution grid does not eliminate the re-circulation of the gas in the upstream part of the hopper. The "variable aperture" grid does appear to improve the gas distribution in both, vertical and horizontal planes.

Some recirculation is still present near the precipitator exit behind the gas distribution grid (see, for example, Figures 5, 7) as it was in the previous CFD study (Report 103-98 A). Overall, the grid does improve gas distribution at the inlet portion of the precipitator. However, its impact diminishes towards the rear (downstream) part of the precipitator.

3.3.5 Summary and Conclusions

The interaction between gas distribution and precipitator physics is complex, and the "conventional" wisdom demands that the gas distribution should be very even, which is mostly based on the precipitator efficiency formulas. In the first filed, where most coarse particles are found, there is no sense in trying to raise the heavy dust fraction to the upper region, as it finally has to be accumulated in the hoppers. This supports as distribution with velocities above average at the lower part of the field. From the second filed, it is the finer particles, which are to be caught, suggesting the gas distribution should be even until the exit from the last field. Particle reentrainment in the lower part of the last field might be swept out in the clean gas duct, and it is recommended that the bottom outlet velocities be below average. Outlet transitions fitted with gas distribution devices make it possible to adjust the vertical velocity profile, which is essentially important in cases where the precipitator is designed with a “bottom-type” outlet.

The hot gas electrostatic precipitator geometry has been analyzed numerically with the help of the Computational Fluid Dynamics (CFD) model. This case includes gas distribution grids at the precipitator inlet and outlet, and several flow direction baffles inside precipitator and in the hopper. It was recommended to use a “variable aperture” or tapered design gas distribution grid at the precipitator inlet with 60% open area at the top gradually converging to 40% open area at the bottom. The purpose of this grid is to redistribute the gas flow in the precipitator upward to assure lower gas velocities at the bottom in the hopper area to further improve overall precipitator collection efficiency.

Furthermore, the CFD simulation allows for calculation of the gas velocity deviation. Hot gas distribution analysis inside the precipitator was also conducted based on the mean gas velocity according to IGCI standards.

These analyses produced the following results:

Location	**Case “A”**			**Case “B”**		
	Deviation, %		**RMS, $ft^2/sec.$**	**Deviation, %**		**RMS, $ft^2/sec.$**
	$1.15V_{av}$	**$1.4V_{av}$**		**$1.15V_{av}$**	**$1.4V_{av}$**	
Front	29.5	21.4	9.32	27.5	20.3	9.29
Back	18.3	9.7		15.4	9.4	

Overall, the grid does improve gas distribution at the inlet portion of the precipitator. However, its impact diminishes towards the rear (downstream) part of the precipitator.

Indeed, application of the “variable aperture” gas distribution device appears to resolve some of the problems with the gas flow distribution inside of the hot gas precipitator. Although the “upward” re-direction of the gas flow did not completely remove the flow recirculation inside the hopper, still, overall positive preponderance is present.

Further improvement could be achieved by addressing area of the small recirculation between the guide vanes in the inlet nozzle (Figure 6). Although the hot gas recalculation is substantially reduced as compared to the Case "A," this phenomenon could be still improved further. However, this refinement should be very carefully monitored from the operational stand point, for the severity of the dust deposits growth in certain areas could defeat improvements in the gas flow distribution.

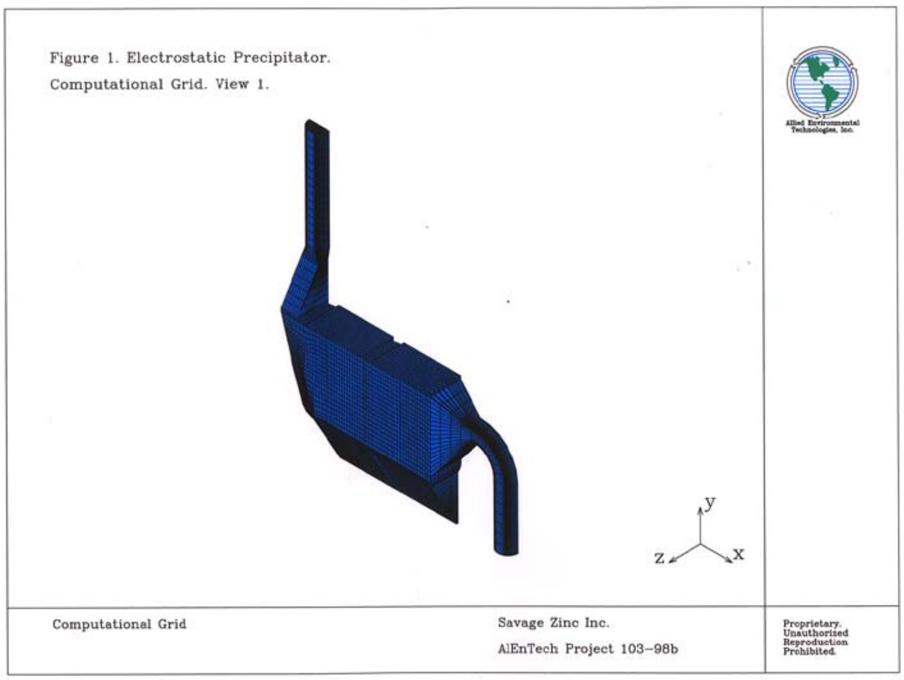

Figure 1. Electrostatic Precipitator.
Computational Grid. View 1.

Figure 2. Electrostatic Precipitator.
Computational Grid. View 2.

Allied Environmental Technologies, Inc.

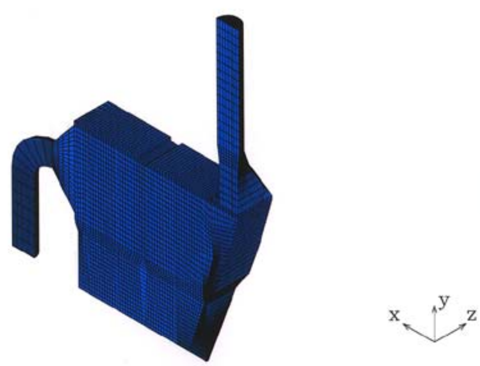

Computational Grid

Savage Zinc Inc.
AlEnTech Project 103–98b

Proprietary. Unauthorized Reproduction Prohibited.

Figure 3. Electrostatic Precipitator.
Internal Computational Details.

Allied Environmental Technologies, Inc.

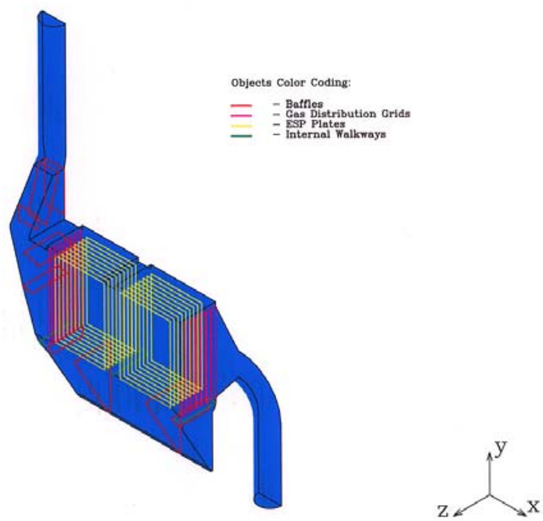

Computational Details

Savage Zinc Inc.
AlEnTech Project 103–98b

Proprietary. Unauthorized Reproduction Prohibited.

Figure 4. Electrostatic Precipitator.
Velocity Vectors Section Numbers.

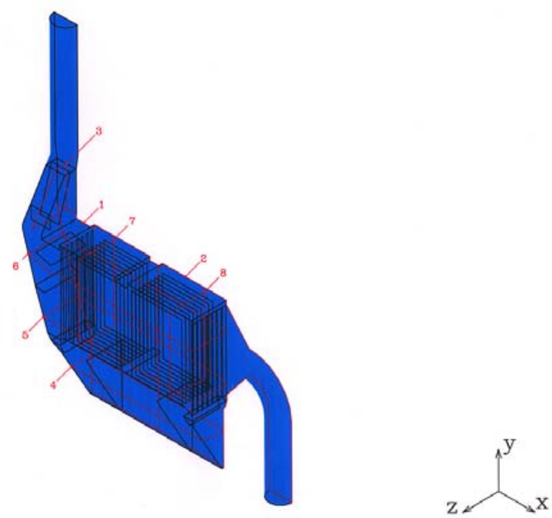

Velocity Vector Sections

Savage Zinc Inc.
AlEnTech Project 103–98b

Allied Environmental Technologies, Inc.

Proprietary. Unauthorized Reproduction Prohibited.

Figure 5. Electrostatic Precipitator. Cental Section Velocity Vectors.

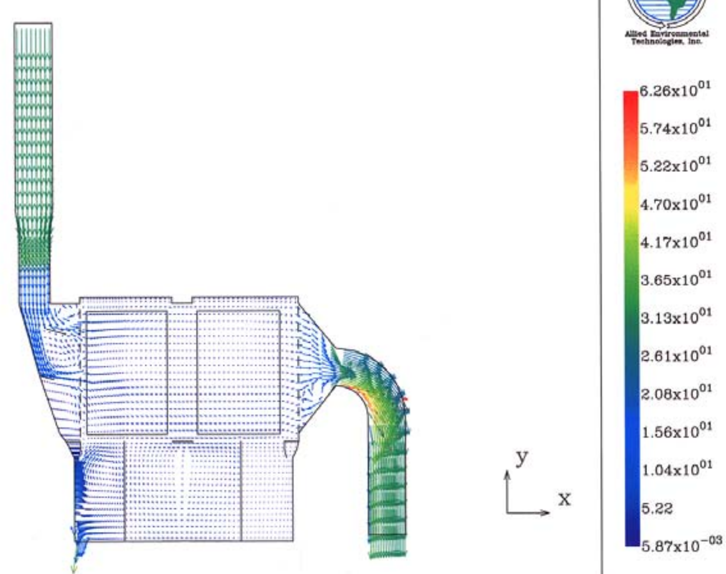

Variable: Velocity Vectors
Units : ft/sec

Local max: $6.26x10^{01}$
Local min: $5.87x10^{-03}$

Savage Zink Inc.
AlEnTech Project 103–98b

Allied Environmental Technologies, Inc.

Proprietary. Unauthorized Reproduction Prohibited.

Figure 6. Electrostatic Precipitator. Section 1 Velocity Vectors.

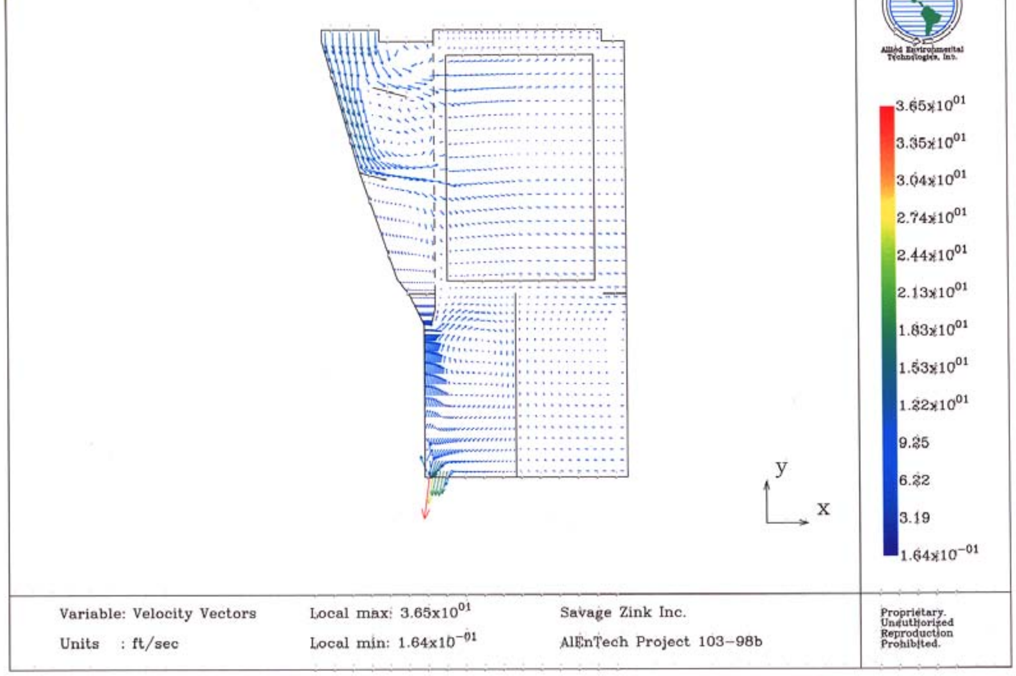

Figure 7. Electrostatic Precipitator. Section 2 Velocity Vectors.

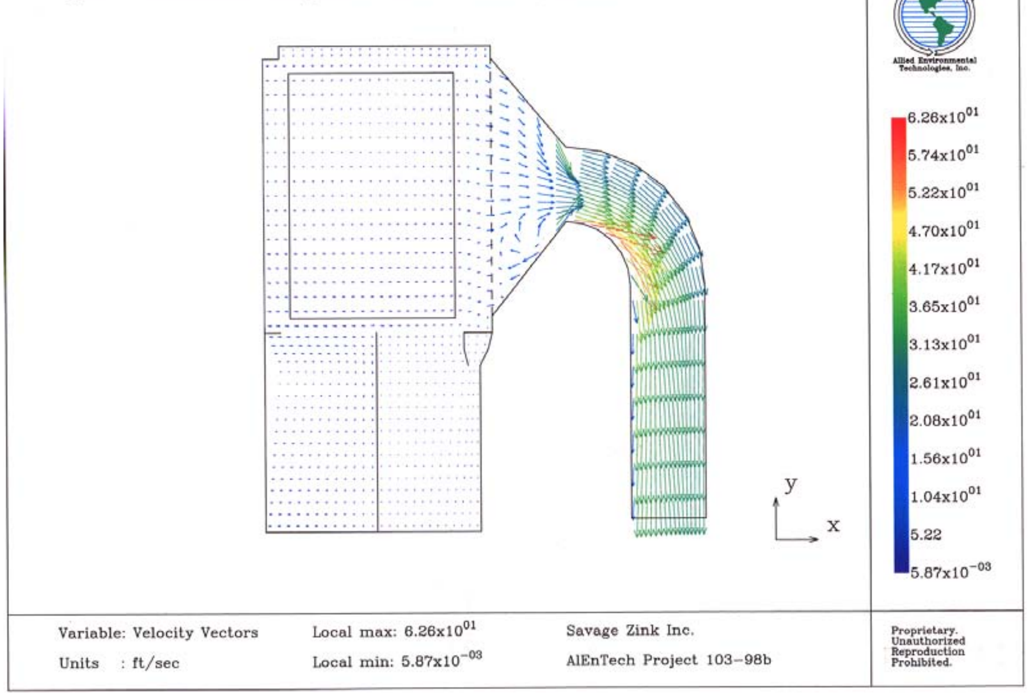

Figure 9. Electrostatic Precipitator. Section 4 Velocity Vectors.

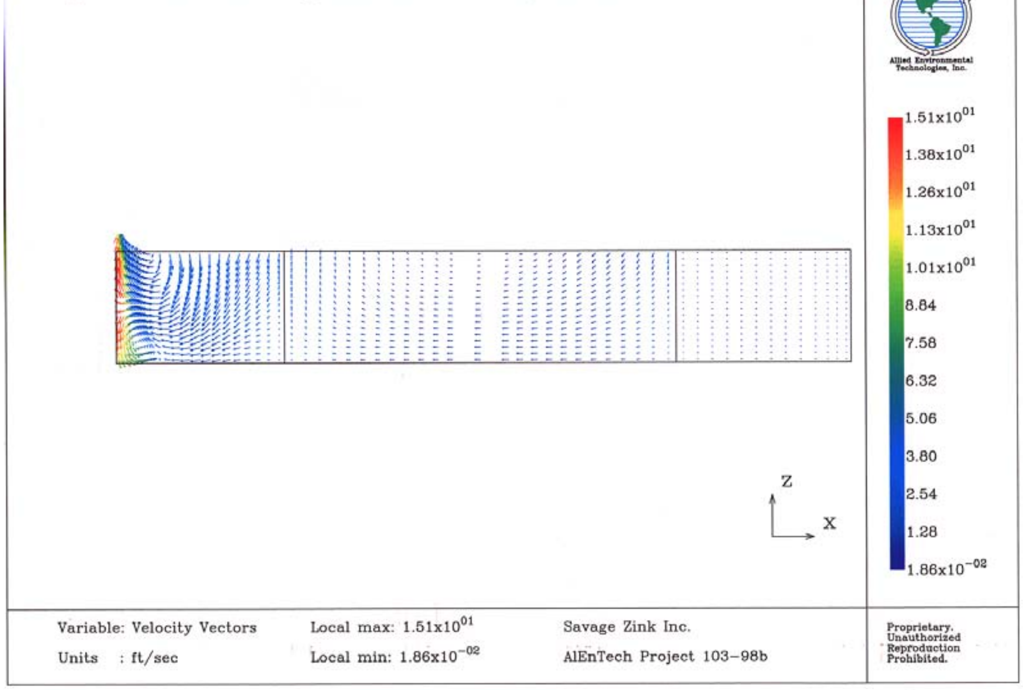

Figure 10. Electrostatic Precipitator. Section 5 Velocity Vectors.

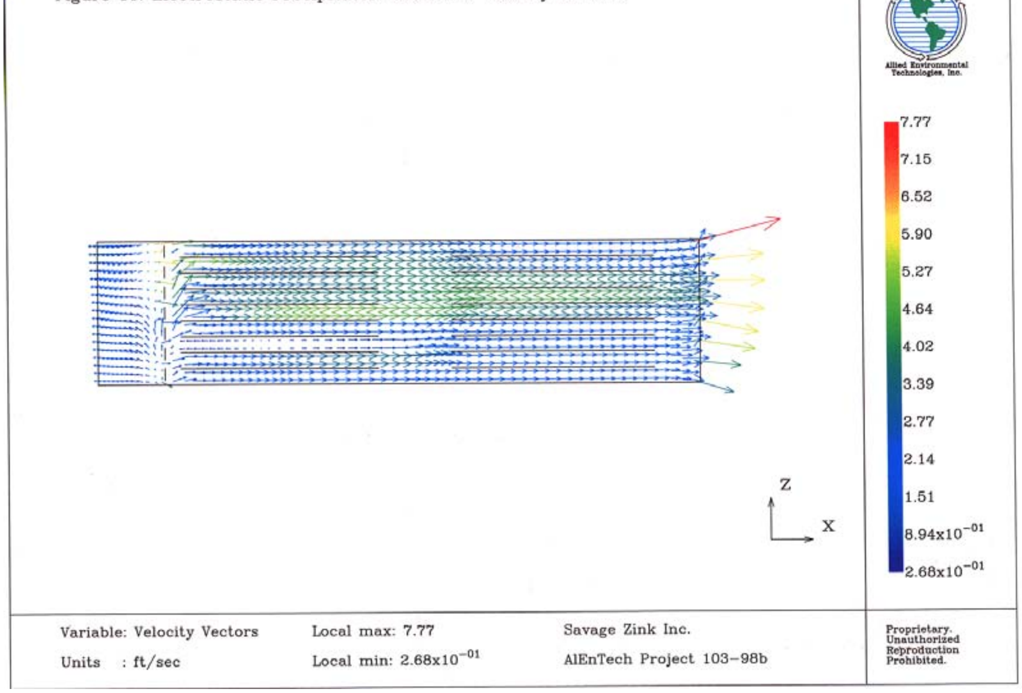

Figure 11. Electrostatic Precipitator. Section 6 Velocity Vectors.

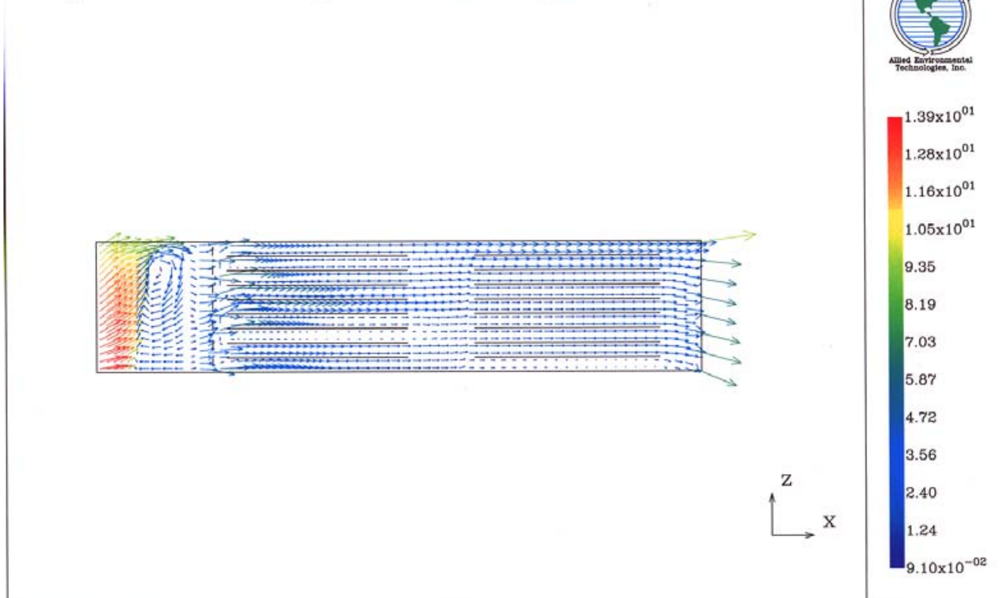

Variable: Velocity Vectors | Local max: 1.39×10^{01} | Savage Zink Inc. | Proprietary. Unauthorized Reproduction Prohibited.

Units : ft/sec | Local min: 9.10×10^{-02} | AlEnTech Project 103–98b

Figure 12. Electrostatic Precipitator. Section 7 Velocity Vectors.

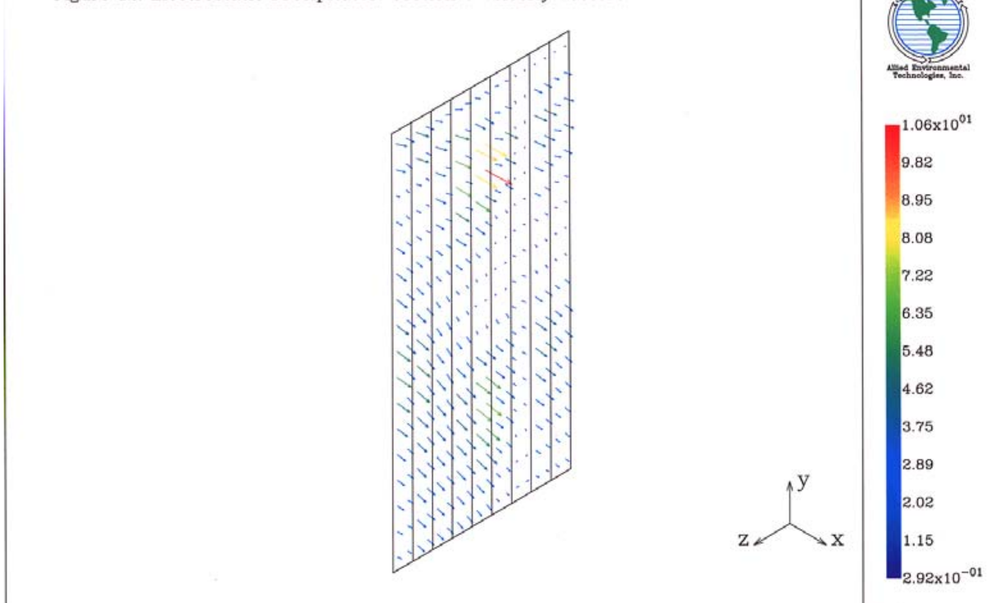

Variable: Velocity Vectors | Local max: 1.06×10^{01} | Savage Zink Inc. | Proprietary. Unauthorized Reproduction Prohibited.

Units : ft/sec | Local min: 2.92×10^{-01} | AlEnTech Project 103–98b

Figure 13. Electrostatic Precipitator. Section 8 Velocity Vectors.

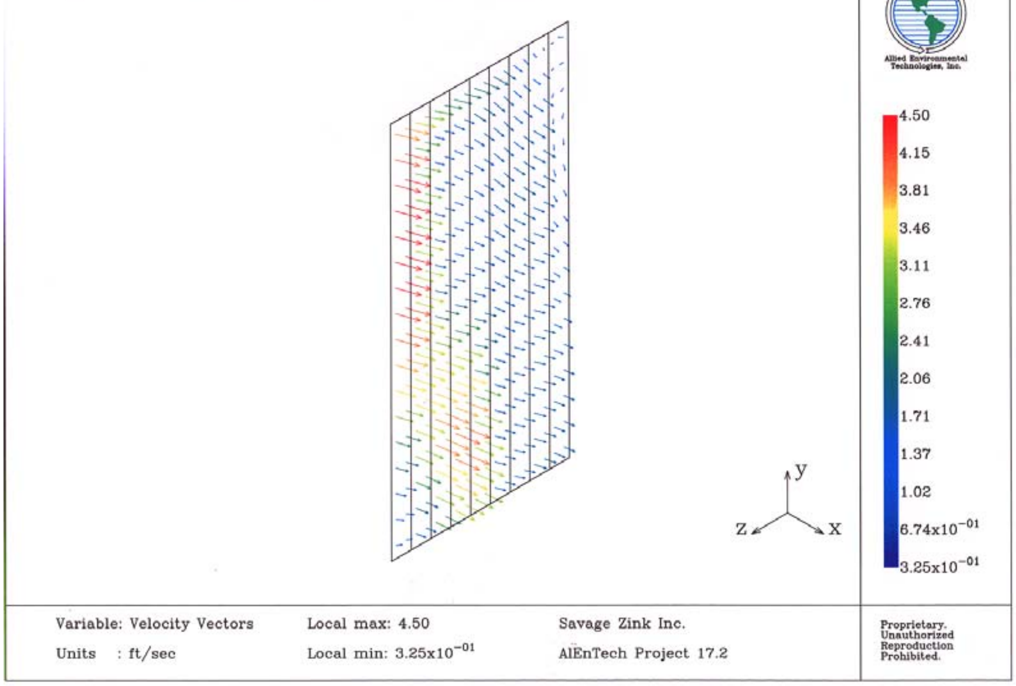

3.4 Air Flow Modeling in the Regenerative Thermal Oxidizer

3.4.1 Packed Tower

The three-dimensional flow in a cylindrical packed tower was simulated using a CFD model. The inside diameter and the height of the packed tower measure 8 and 12 feet respectively. The gas flow rate in the packed tower was rated at 10,000 scfm (at 70 °F). The actual gas temperature at the bottom and the top of the packed tower was assumed 213 °F and 1,400 °F respectively.

In the CFD model, the packed tower was represented by 8,424 (18x26x18) cells. The model included the randomly packed media, the off-centered inlet duct (nozzle), and the exit ductwork as depicted in the Figure 1.

A uniform mean temperature of 807 °F was assumed throughout the packed tower in the calculation to account for the temperature effect of the gas. The randomly packed media was simulated as porous material with permeability specified according to conditions provided by the Smith Engineering, i.e. that the overall pressure loss across the 7 (seven) feet deep media shall be 7 inches of water column (WC) at the rated gas flow.

3.4.2 Results

The computed mass flux vectors are plotted in Figures 2 through 4 for three vertical planes in the tower. These results show that the mass flux inside of the packed bed (between the two horizontal dashed lines is fairly uniform. According to numerical values, the variation of the mass flux in the media is less than 7% of the mean flux.

The mean temperature of 807 °F was assumed throughout the calculation, and the exact volumetric gas flow rate cannot be accurately calculated, the mass flux still is a conservative quantity regardless of the constant temperature assumptions. The uniform mass flux in Figures 2 through 4 implies uniform velocity profile provided that the temperature is uniform in a horizontal cross section through the packed bed.

Figure 5 depicts the smoke trails corresponding to the flow paths in the packed tower. The swirling for pattern at the bottom of the tower is due the off-centered inlet duct (nozzle) design.

Figure 6 shows the calculated pressure distribution across the packed bed. The pressure differential across the entire bed (0.243 psi or 6.73 in. WC) is consistent with the draft loss in the actual tower (7 in. WC)

3.4.3 Summary and Conclusions

A CFD model has been developed for he packed bed tower with the off-centered inlet duct. Preliminary computational results show that with an overall pressure drop of 7 (seven) inches of WC, the mass flow through the packed bed is uniform. According to numerical values, the variation of the mass flux in the media is less than 7% of the mean flax.

3.4.4 Figures

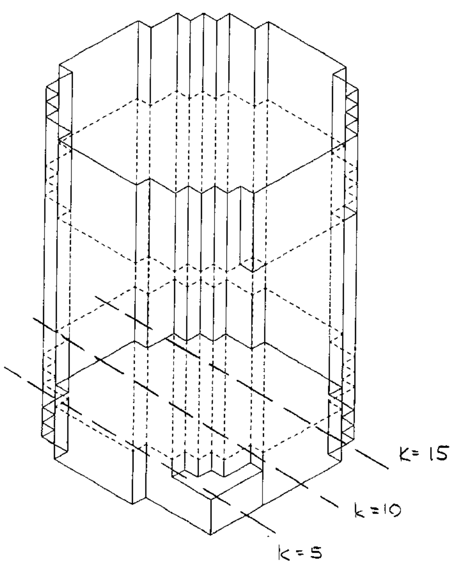

Figure 1. Computational Model Geometry

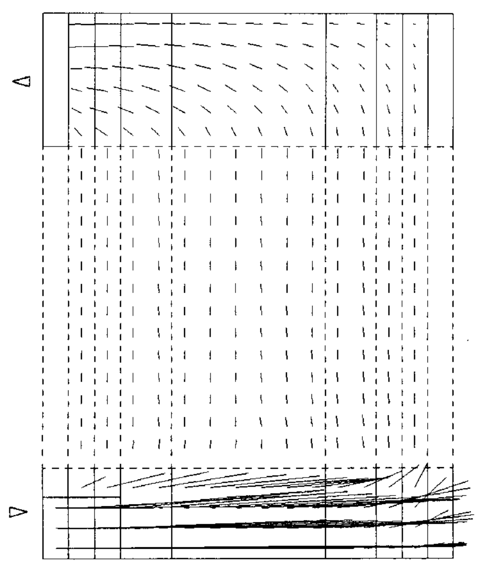

Figure 2. Mass-Flux Vector Plot @k=5

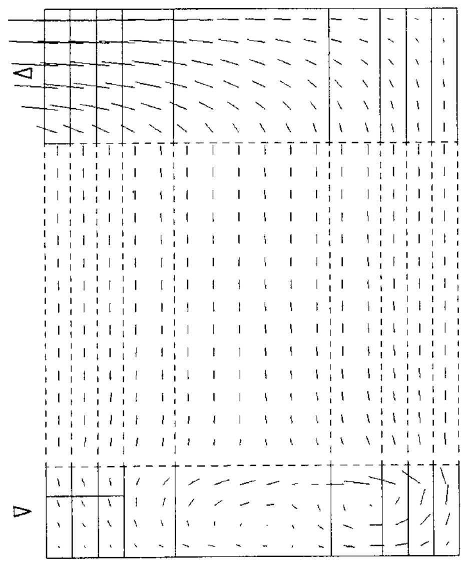

Figure 3. Mass-Flux Vector plot @k=10

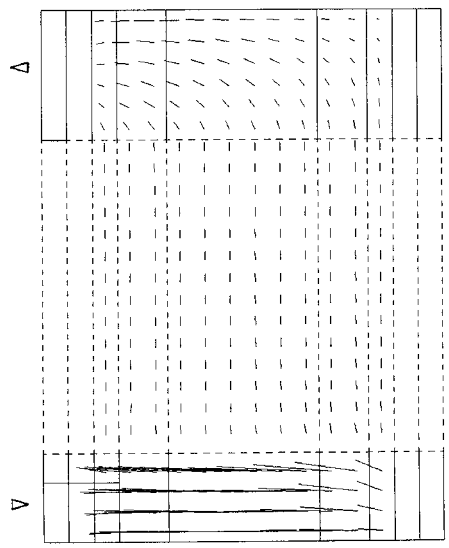

Figure 3. Mass-Flux Vector plot @k=15

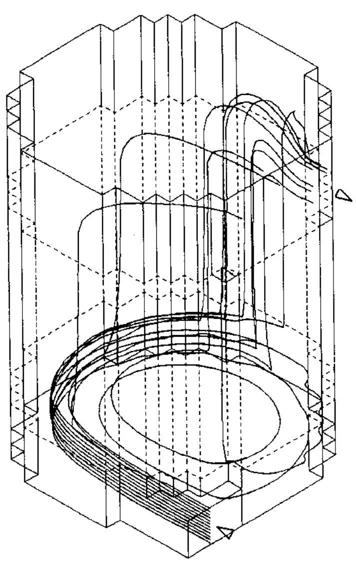

Figure 5. Smoke Trails

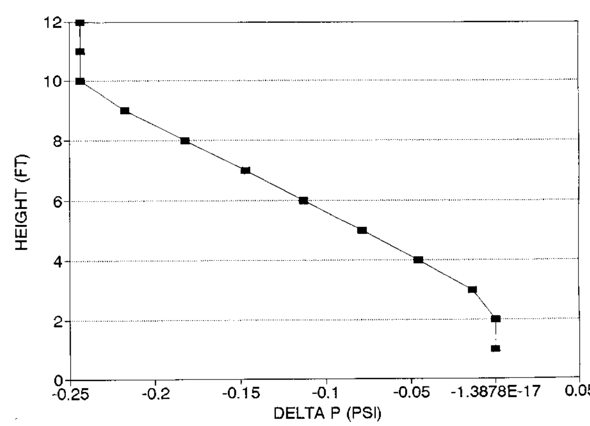

Figure 6. Pressure Distribution in the Packed Tower

3.5 Model Study for In-Duct Burners

3.5.1 Model Set-up

The CFD model was run in a conventional mode to evaluate the gas patterns, velocity vectors, pressure parameters, combustion products, as well as oxygen and NO_x formation characteristics.

3.5.2 Discussion

Figures 1 through 12 depict the results of the CFD modeling in the two cross-sections:

1. Cross-Section I - along the center line (C/L) of the orifice and a larger hole.

2. Cross-Section II - along the center of the smaller holes, and

3. Cross-Section III - ½ of the plane perpendicular gas flow at the end of the duct.

Figure 1 represents results of the thermal NO_x calculations in the Cross-Section I. The units are mass fraction in kg/kg, i.e. thermal NO_x fraction in kg in total gas flow in kg. Figure 2 depicts the same values along in the Cross-Section II.

Figure 3 depicts the Static Pressure in Pascal in the Cross-Section I, and the Figure 4 represents the results of the gas density calculations, in kg/m^3 in the same cross-section.

Figures 5 and 6 depict the results of the absolute temperature calculations in °K.

Figures 7 through 10 depict the Velocity Vectors in Cross-sections I and II in m/sec. Figures 9 and 10 represent blow-up views to help identify the flow patterns through the openings in the strands. Although the gas exit profile looks relatively uniform, it could be seen, that there are areas with extremely high gas velocities virtually completely by-passing the combustion zones, thus allowing one to suspect the efficiency of the VOC's destruction on those areas (obviously, making an impact on the overall VOC destruction efficiency). Compare those with the Figure 11, one can see that the gas flow by-passes the high temperature zones and converges back with the main portion of the gas in the much cooler zone on the far left side of the plane (in reality it represents let's say a top portion of the duct). Perhaps, extending the strands a little bit more could improve the flow pattern and, respectively overall VOC destruction efficiency.

3.5.3 Figures

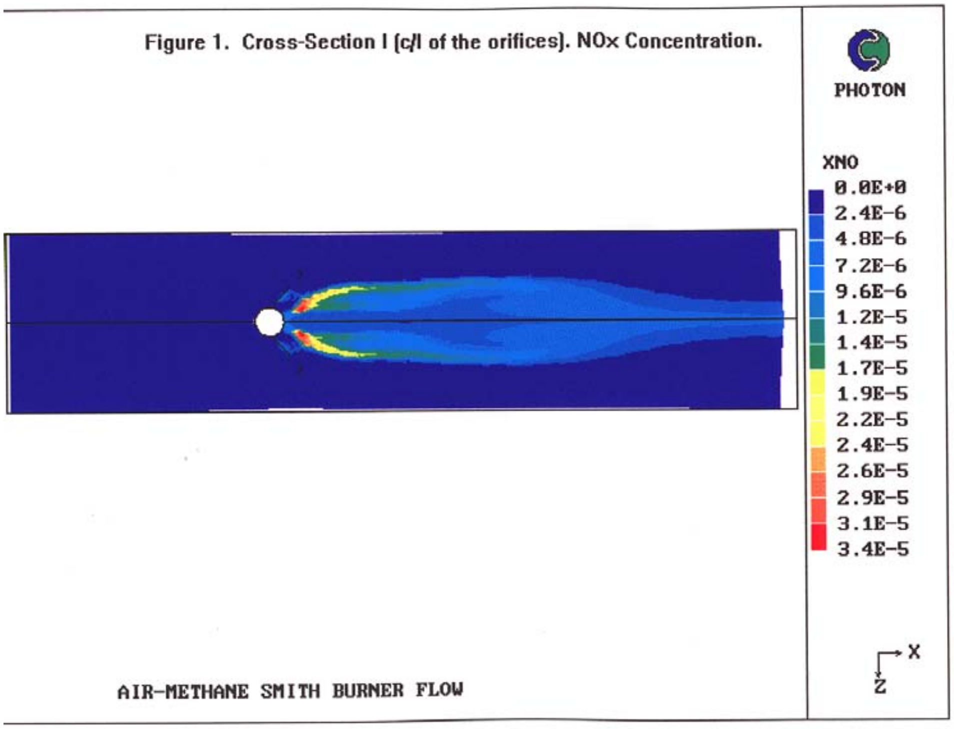

Figure 1. Cross-Section I (c/l of the orifices). NOx Concentration.

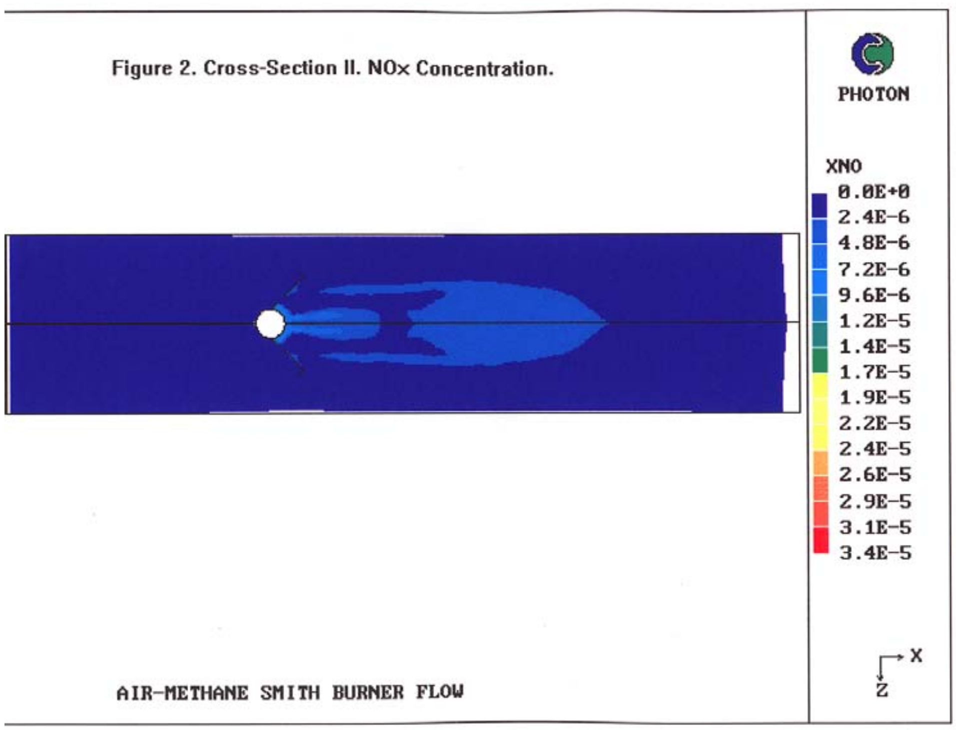

Figure 2. Cross-Section II. NOx Concentration.

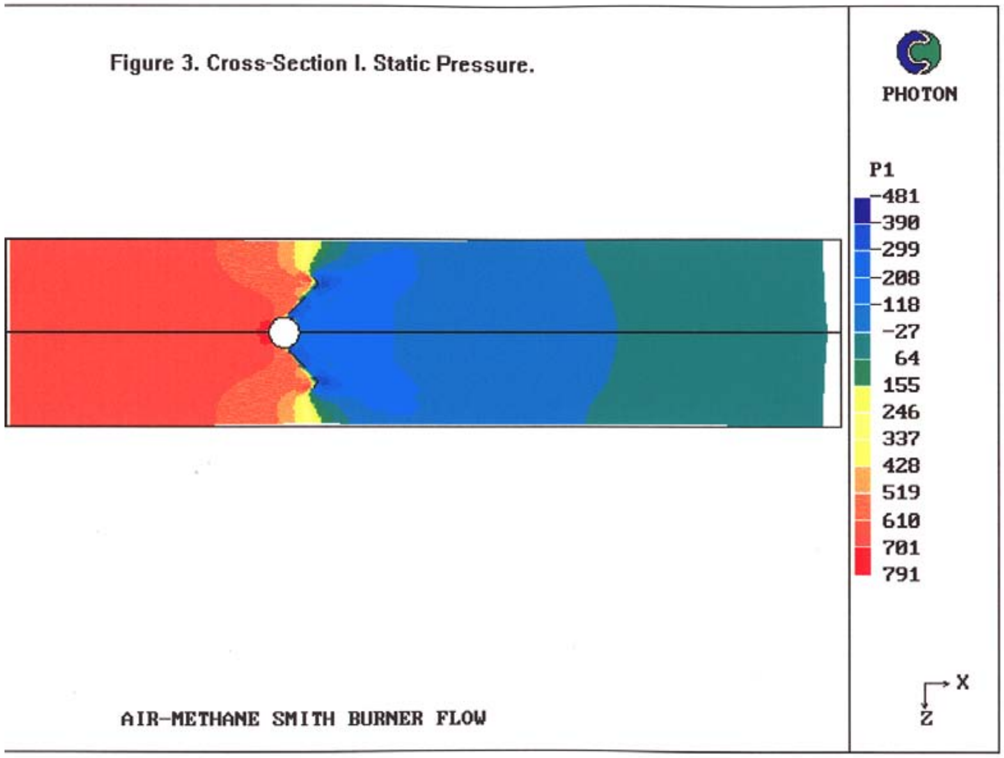
Figure 3. Cross-Section I. Static Pressure.
PHOTON
P1
-481
-390
-299
-208
-118
-27
64
155
246
337
428
519
610
701
791
AIR-METHANE SMITH BURNER FLOW
X
Z

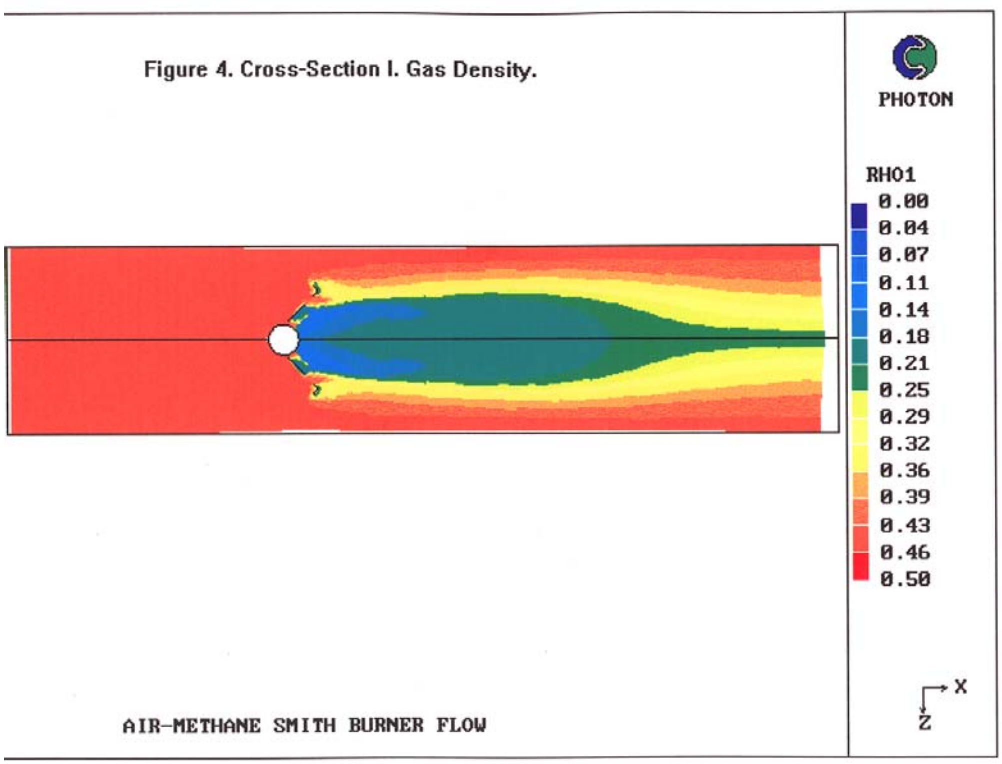
Figure 4. Cross-Section I. Gas Density.
PHOTON
RHO1
0.00
0.04
0.07
0.11
0.14
0.18
0.21
0.25
0.29
0.32
0.36
0.39
0.43
0.46
0.50
AIR-METHANE SMITH BURNER FLOW
X
Z

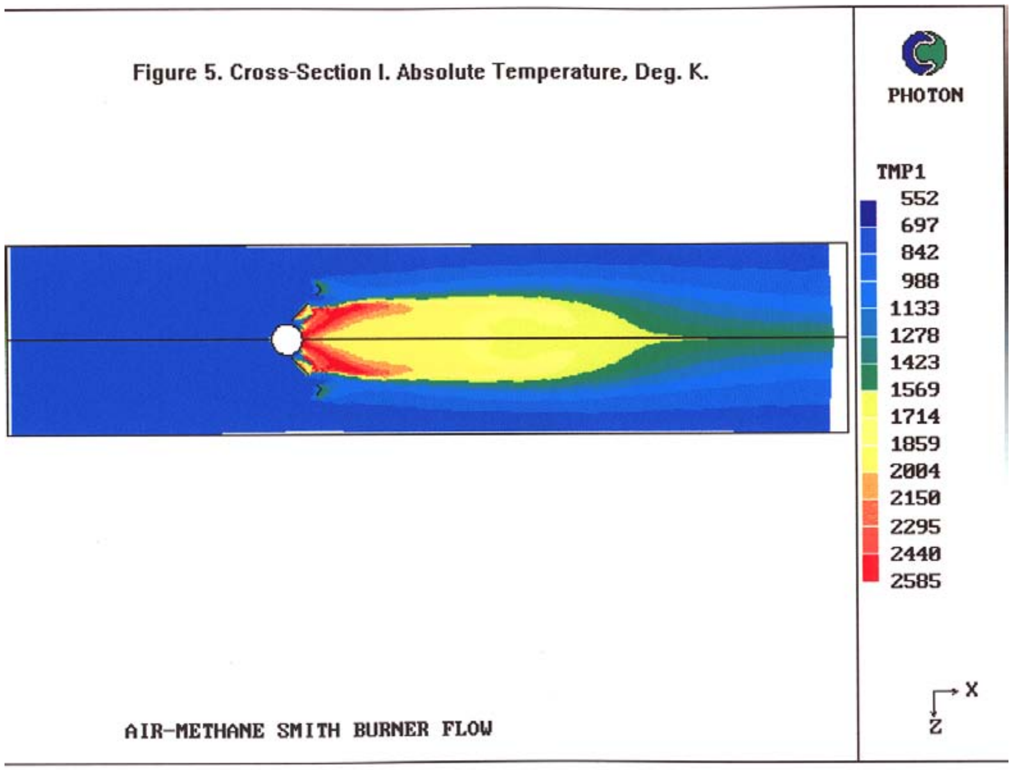

Figure 5. Cross-Section I. Absolute Temperature, Deg. K.

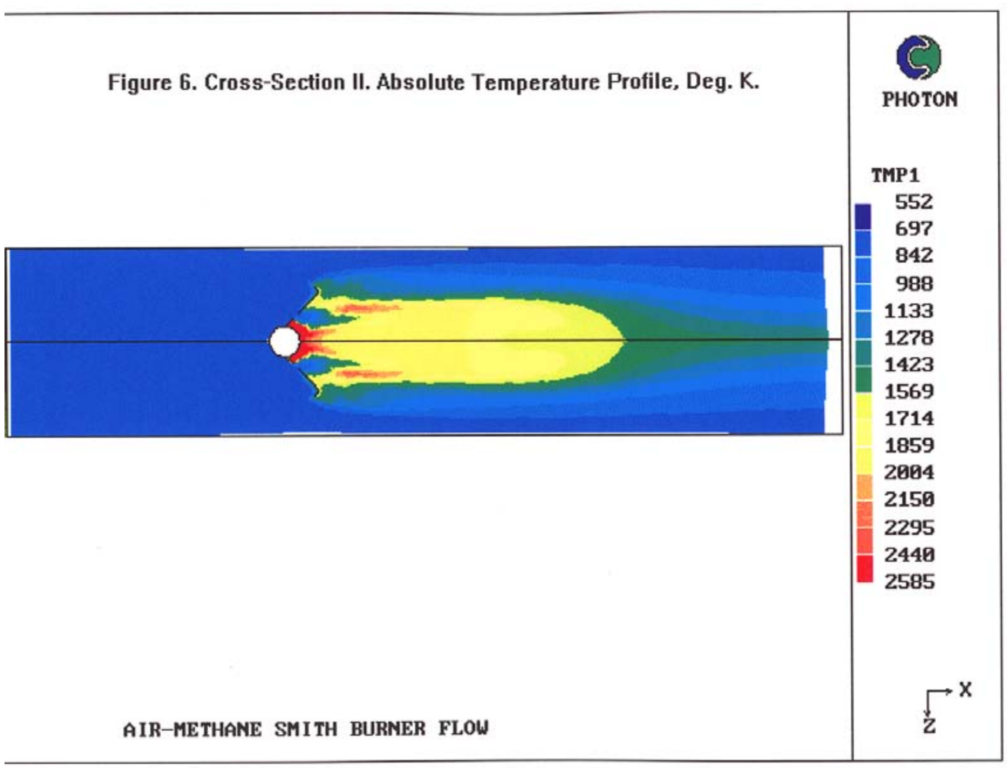

Figure 6. Cross-Section II. Absolute Temperature Profile, Deg. K.

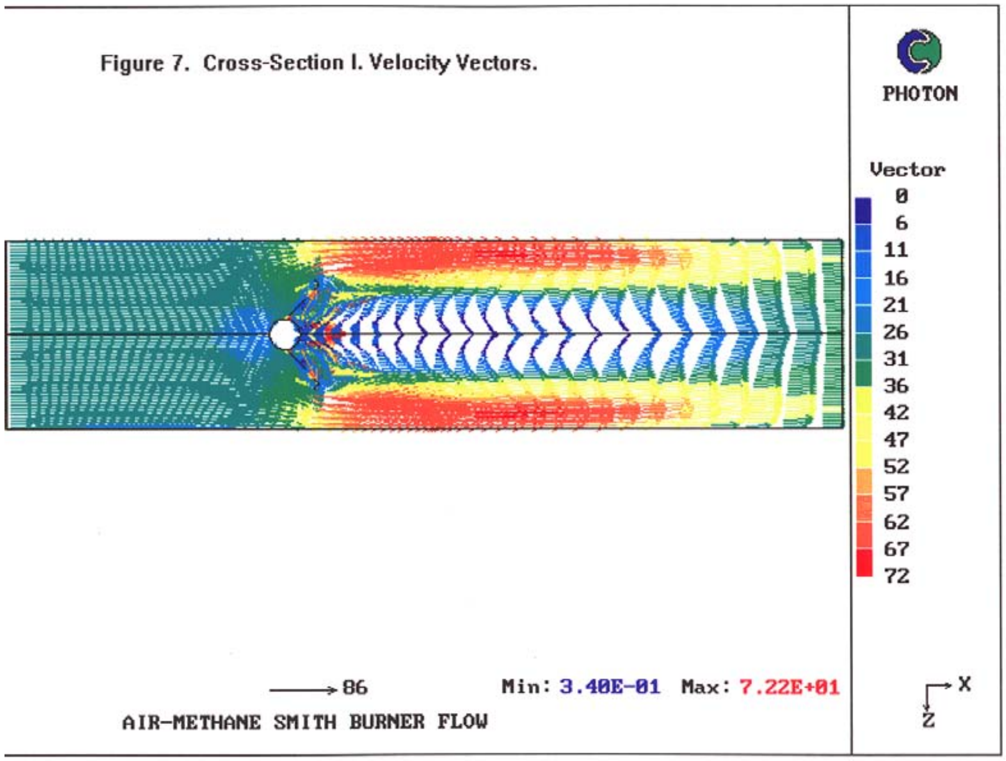

Figure 7. Cross-Section I. Velocity Vectors.

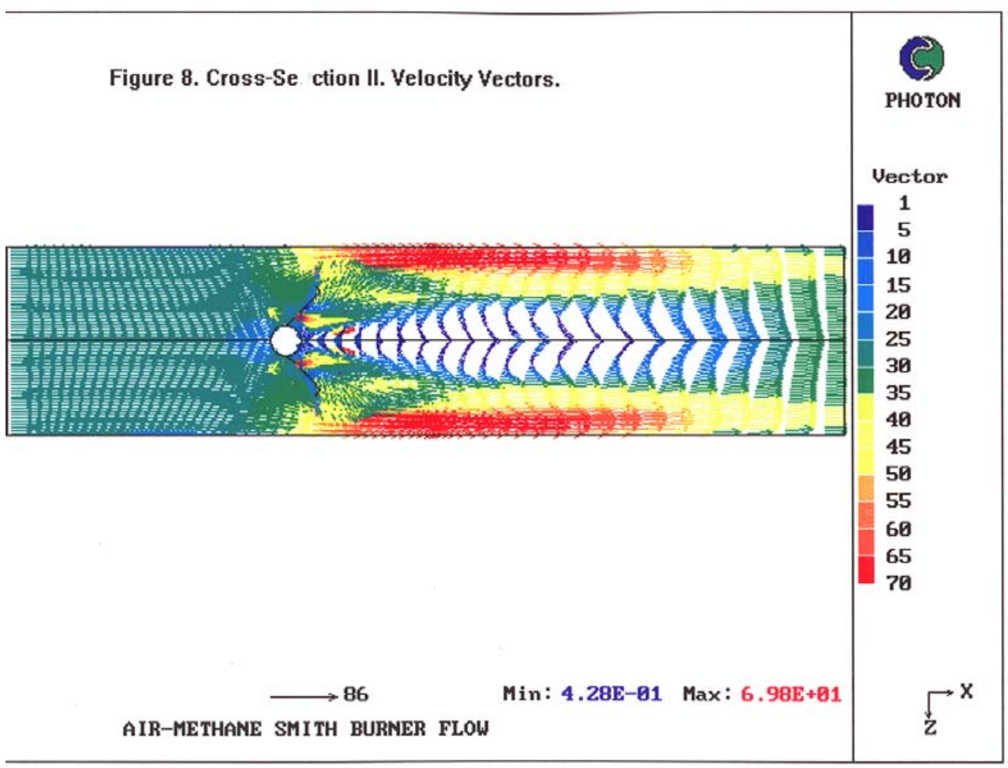

Figure 8. Cross-Se ction II. Velocity Vectors.

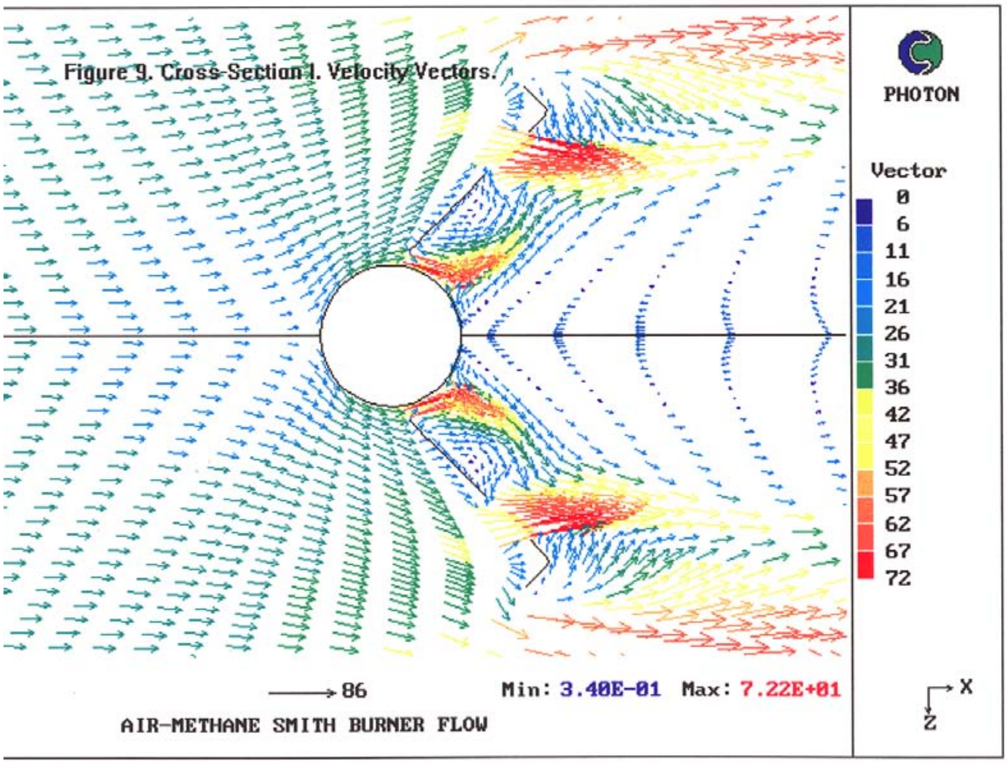
Figure 9. Cross-Section I. Velocity Vectors.
PHOTON
Vector
0
6
11
16
21
26
31
36
42
47
52
57
62
67
72
86
Min: 3.40E-01 Max: 7.22E+01
AIR-METHANE SMITH BURNER FLOW
X
Z

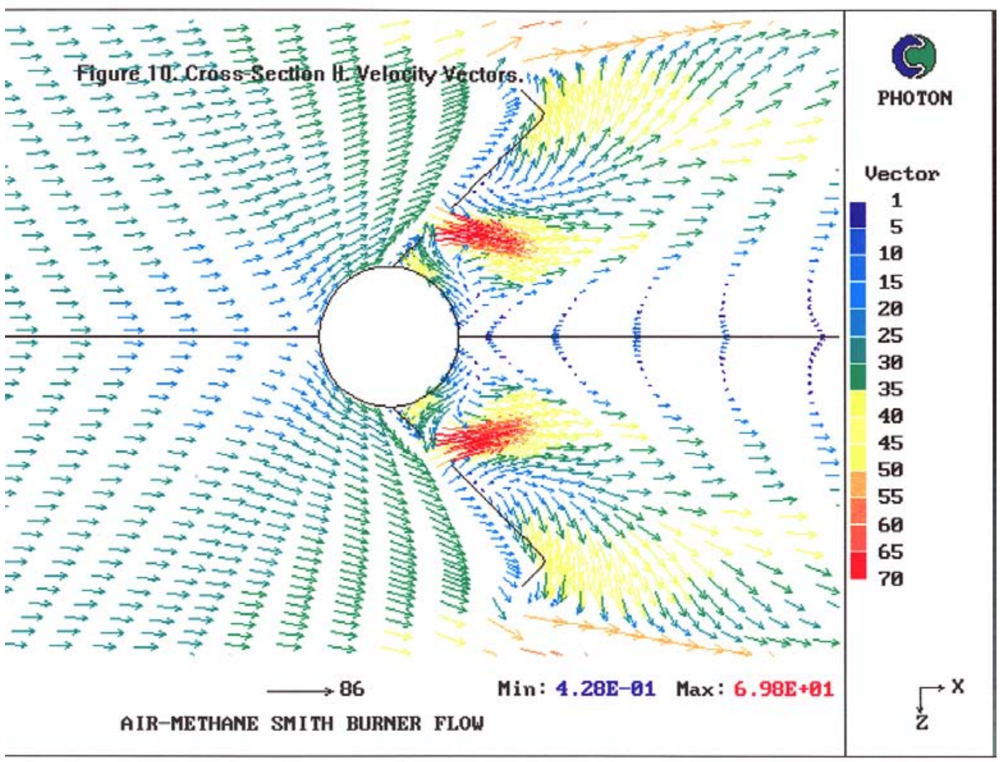
Figure 10. Cross-Section II. Velocity Vectors.
PHOTON
Vector
1
5
10
15
20
25
30
35
40
45
50
55
60
65
70
86
Min: 4.28E-01 Max: 6.98E+01
AIR-METHANE SMITH BURNER FLOW
X
Z

3.6 Lindberg Incinerator and Absorption Tower Flow Evaluation

3.6.1 Model Setup

The CFD software package was utilized to analyze the flow of the exhaust gas throughout an Absorption Tower system. The Chen-Kim κ-ε model of the turbulent flow was applied for these tasks. This model provides the time-averaged values of velocities and pressure of the air throughout the system. It has become one of the most popular two-equation model of turbulence, though mostly for historical rather than scientific reasons. The model calculates the effective viscosity associated with the turbulence based on the solution of two equations for the density of turbulent kinetic energy k and rate of the dissipation of this energy ε. Like other two-equation models, the κ-ε model is free from the need to prescribe the length-scale distribution. Although it does necessitate the solution of two additional differential equations, these are of the same form as the momentum equation; Fluent (like other modern computer codes) solves them easily.

The high-Reynolds number κ-ε model becomes invalid near the walls and thus has to be regarded with the set of wall functions (low-Reynolds number models are also available but rarely used in engineering community). The logarithmic wall functions have been used here; these functions are applicable for the Reynolds numbers based on the length of the system, which are in the range from approximately 10^6 to 10^9. The analysis of the Absorption Tower shows that this is true for almost all system considered. The surfaces of the Absorption Tower are assumed smooth.

The other boundary conditions applied are fixed mass flow rate at the entrance to the system and fixed pressure at the exit from the system. The inlet boundary conditions require the prescription of the two turbulent parameters, density of the kinetic energy of turbulence κ and rate of the dissipation of this energy ε. The unknown values can be solved for an assumed intensity of the turbulence at the entrance. This allows us determine the value of κ, the value of ε is than determined based on the inlet linear dimensions. Typical inlet turbulence intensity is between 1% and 5%, with the high value of 5% has been chosen for our calculations.

The equation of state of exhaust gas was assumed the one of the constant density gas. This assumption is valid since the static pressure drop through the system is of order of 1 inch of water, this value is less than 1% of the atmospheric pressure, and the expected density change is about one percent. The inlet mass flow rate of the gas and its temperature and chemical composition has been provided by the customer. The kinematic viscosity of the gas at the given conditions has been determined using the Sutherland's formula and was assumed to be the constant throughout the system.

Three configurations (Cases A through C) of the Absorption Tower were considered. The first configuration, Case A (details of this configuration are shown on Figure 2) is the original one, which includes the extension of the inlet tube inside tower. The second configuration (Case B, Figure 2) represents modification where inlet tube ends at the tower entrance, and three direction plates and ring and plate with holes are present inside the tower. The third configuration (Case 3, Figure 2) was proposed by the customer. This configuration is similar to the Case B configuration with the exception that perforated ring is absent and perforated plate occupies the whole cross-section of the tower. The perforated plates were modeled as porous material with given pressure loss coefficient, this coefficient was determined based on the results of publication *G.B.Schubauer, W.G.Spangenberg and P.S.Klebanoff, Aerodynamic Characteristics of Damping Screens, NASA TN 2001, January 1950.*

The computational mesh has been constructed using the specifications provided by the customer with utilizing the Fluent body-fitted coordinates approach, which allows the creation of the grid of complex geometry. It contains 24x14x110 cells (Figure 1). Due to the symmetry of the Absorption Tower with respect to the central vertical plane, only half of the exhaust stack was simulated in order to reduce the computational time.

3.6.2 Results and Discussion

The results of the CFD simulations have been provided in the form of velocity vectors through different sections of the Absorption Tower (Figures 3-8 for the Case A, Figures 11-16 for the Case B Configuration and Figures 19-24 for the Case C Configuration). The computational mesh for the case considered is also presented (Figure 1).

As it could be seen from the figures that the gas flow inside the Absorption Tower is very complex one with several recirculation zones present. For the original configuration, the flow recirculates in vertical direction at the bottom of the column, just above the inlet tube (level of the bottom injection nozzle) and near the exit from the tower (this recirculation may not present in real tower due to presence of baffles near the tower exit which are not present in the simulation). In addition to that, the flow also recirculates in horizontal direction.

The addition of directional plates, removal of inlet tube projection inside tower and addition of the perforated ring and plate in the Case B configuration do alter these recirculation zones, but do not eliminate either of them. Due to high solidity of the perforated plate and ring big portion of the gas flow go around them, which increases the recirculation above the plate.

The best in terms of absence of the flow recirculation among the cases considered is the configuration proposed by the customer. This configuration does not eliminate the recirculation near the bottom of the tower in both horizontal and vertical direction, but does eliminate the recir-

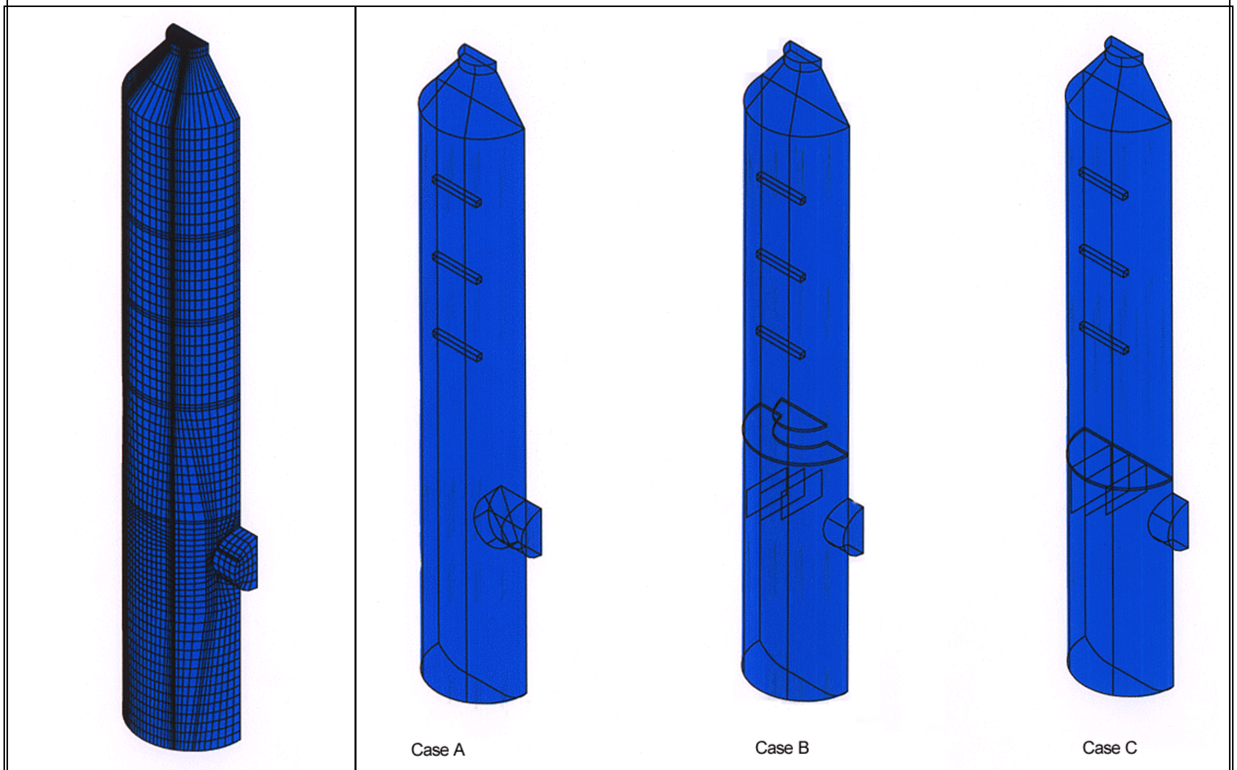

culation in this direction in the injection nozzle area.

3.6.3 Conclusions

The CFD simulation allowed inexpensively determine that among three configurations considered, the configuration presented in the Case C delivers the best distribution of the gas flow near the injection nozzles.

3.6.4 Figures

Computational Grid	Computational Details

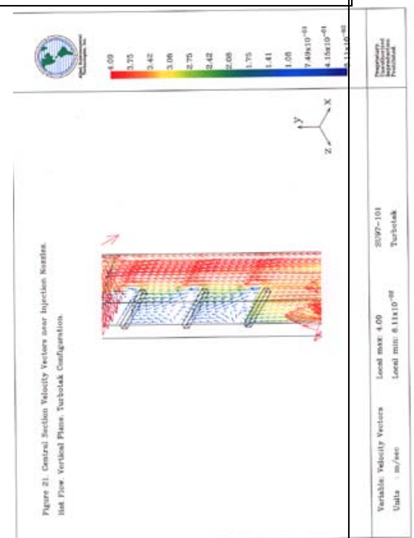

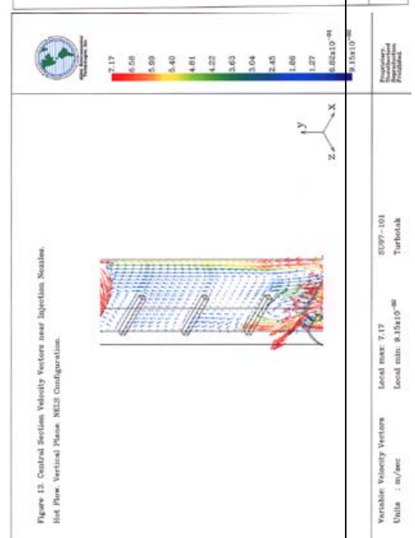

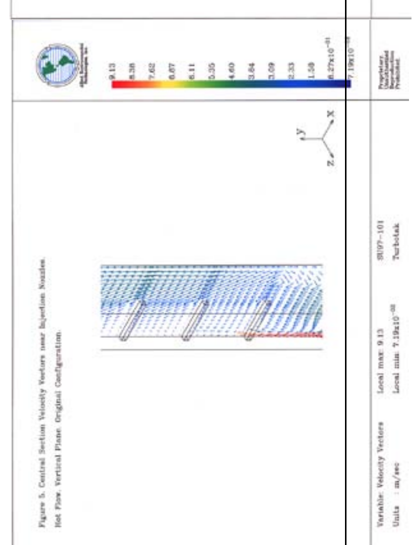

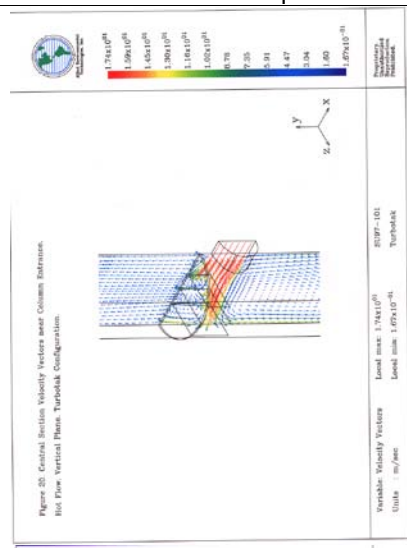

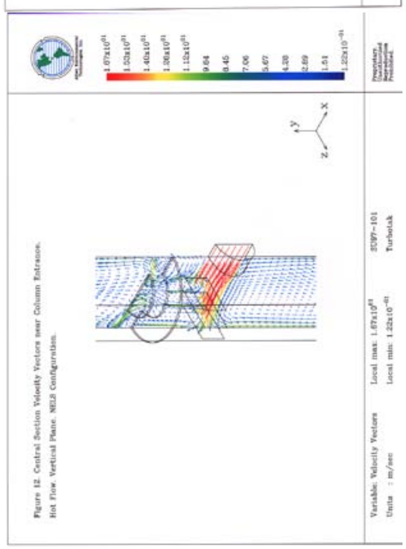

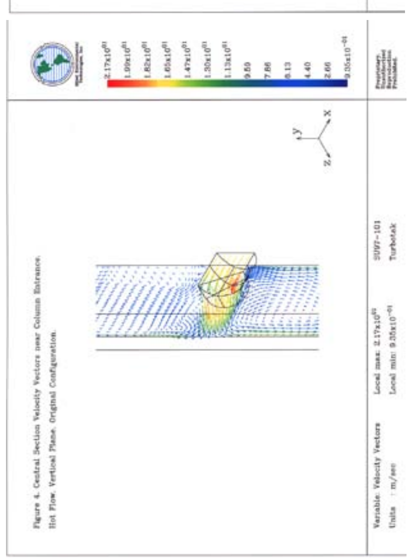

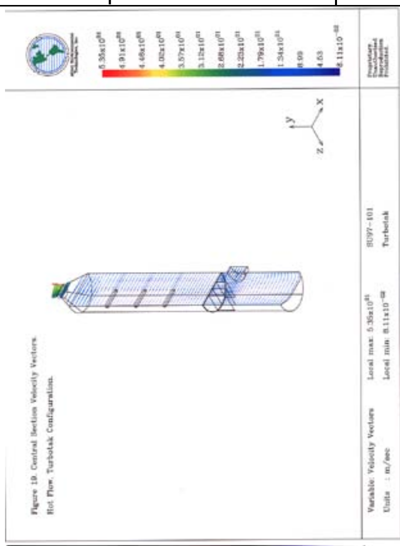

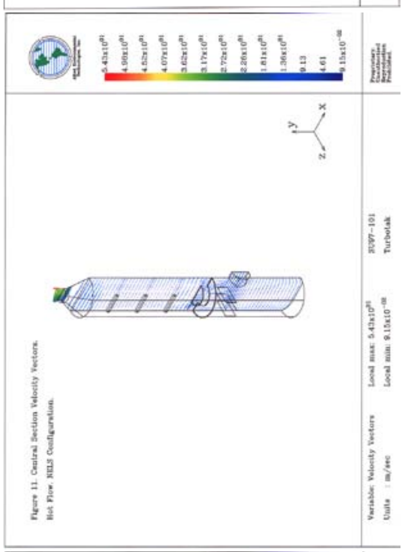

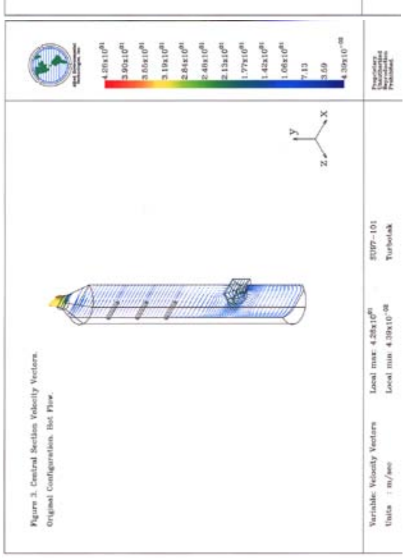

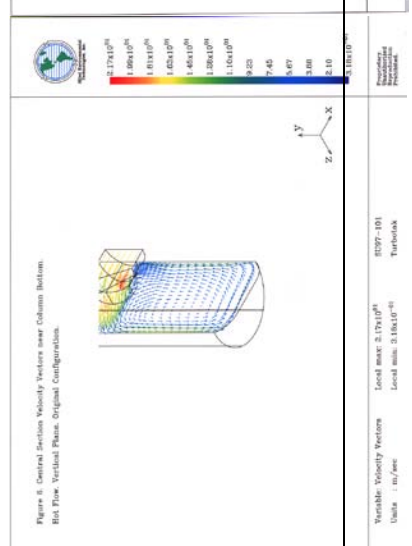

Figure 6. Central Section Velocity Vectors near Column Bottom. Hot Flow. Vertical Plane. Original Configuration.

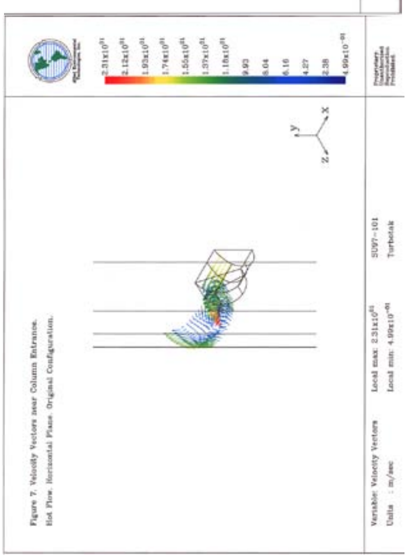

Figure 7. Velocity Vectors near Column Entrance. Hot Flow. Horizontal Plane. Original Configuration.

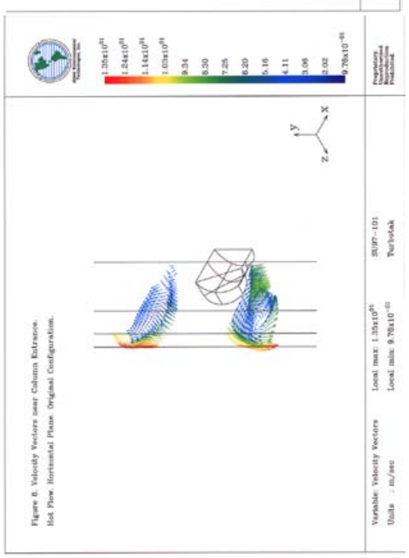

Figure 8. Velocity Vectors near Column Entrance. Hot Flow. Horizontal Plane. Original Configuration.

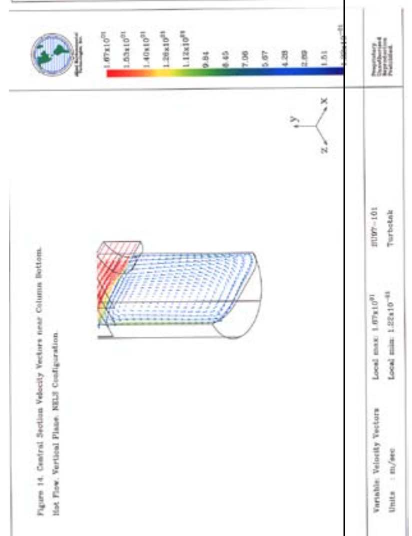

Figure 14. Central Section Velocity Vectors near Column Bottom. Hot Flow. Vertical Plane. NELS Configuration.

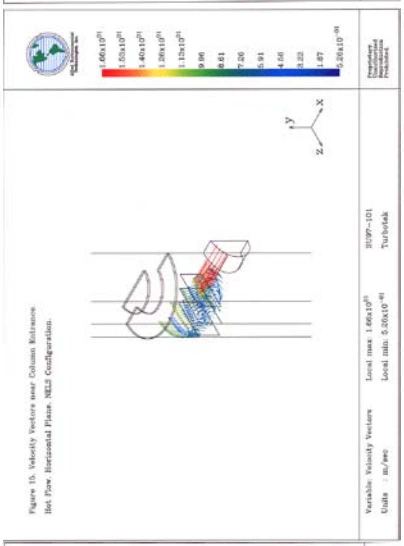

Figure 15. Velocity Vectors near Column Entrance. Hot Flow. Horizontal Plane. NELS Configuration.

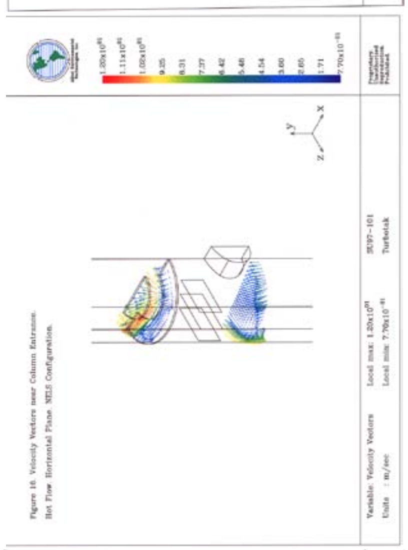

Figure 16. Velocity Vectors near Column Entrance. Hot Flow. Horizontal Plane. NELS Configuration.

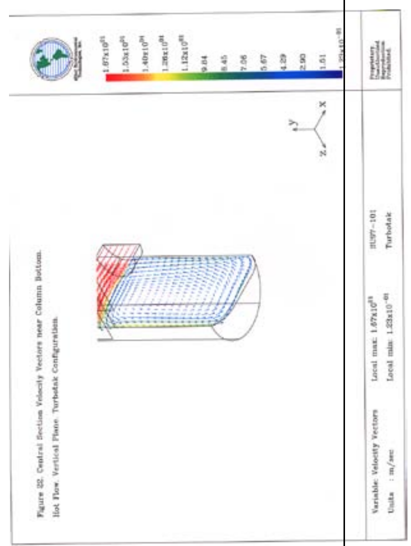

Figure 22. Central Section Velocity Vectors near Column Bottom. Hot Flow. Vertical Plane. Turbotak Configuration.

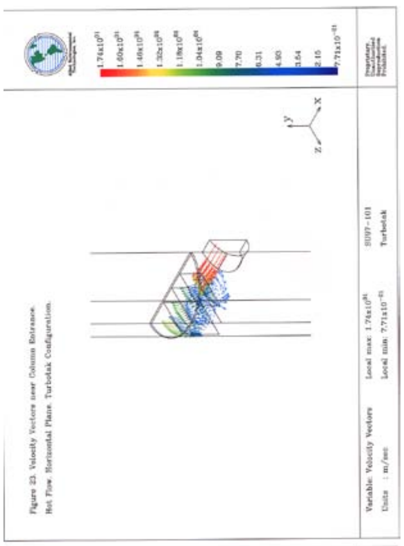

Figure 23. Velocity Vectors near Column Entrance. Hot Flow. Horizontal Plane. Turbotak Configuration.

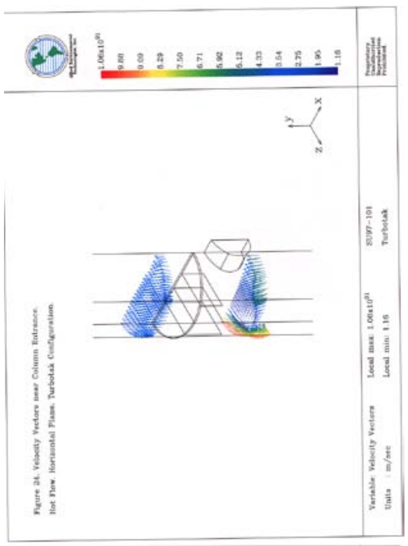

Figure 24. Velocity Vectors near Column Entrance. Hot Flow. Horizontal Plane. Turbotak Configuration.

ONTARIO POWER GENERATION NANTICOKE GENERATION STATION PRECIPITATOR IMPROVEMENT PROJECT

Thomas L. Lumley, OPG Nanticoke GS[i]
Marc D. Voisine P. Eng., Neill & Gunter[ii]
Dr. Henry V. Krigmont, QEP, Allied Environmental Technologies, Inc.[iii]

1 INTRODUCTION

Ontario Power Generation (OPG) owns and operates the Nanticoke coal-fired generating station (Nanticoke GS), which is located on the North shore of Lake Erie in Haldimand County. The station, originally built in the early 1970's, consist of eight (8) units. The units were originally designed for 505 MW (gross) at maximum continuous rating while firing high-sulfur bituminous coal and currently have an adjusted output of 490 MW (gross) based on the approved fuel plan of a blend of Eastern Appalachian low sulfur and PRB coals. All units are equipped with electrostatic precipitator (ESP) to collect fly ash.

During the 1980's OPG was faced with reducing sulfur dioxide emissions at the Nanticoke GS to comply with the new environmental regulations. After careful review of available technologies and strategies, the station chose to switch to a coal blend of <1% sulfur (S) to achieve the desired reduction in sulfur emissions. Subsequently, Nanticoke GS had to employ dual flue gas conditioning (Dual FGC) to inject controlled amounts of sulfur trioxide (SO_3) and ammonia (NH_3) so that existing ESP's could cope with the high resistivity fly ash resulted from firing low sulfur coal blend. Additionally, ammonium sulfate and ammonium bisulfate byproducts helped to improve the fly ash agglomeration and an inter electrode space charge, which helped to further enhance the ESP's performance.

When the FGC systems were installed, it was determined to only employ the FGC on the outlet of the two Secondary Air Heaters (SAH) upstream of the precipitators. It was decided at the time not to condition the flue gas flow exiting the Primary Air Heater (PAH), which represents approximately 20% of the flue gas flow. At the time, there was concern that the flue gas temperatures exiting the primary air heater were sufficiently low enough that corrosion could become an issue if sulphur trioxide were injected into this gas stream. Therefore, 20% of the flue gas flow entered the precipitator unconditioned with a corresponding impact on the particulate capture efficiency.

2 BACKGROUND

In late 2005 the Nanticoke GS engineering and project group explored opportunities to improve the overall particulate capture efficiency of the existing precipitators. This could be accomplished by upgrading the existing precipitators with additional collection area, rigid discharge electrodes (RDE), new collecting plates, new T/R sets, new rappers and new controls. The study also identified two potential modifications to the current FGC systems that would be key to the particulate capture improvement program. The first recommended that FGC injection probes be installed on the primary flue gas flow to ensure 100% of the flue gas is conditioned prior to entering the precipitator. Although, not installed originally because of corrosion concerns, it was agreed that the flue gas temperatures with the current fuel burn are higher than the original 1980's study and therefore corrosion may not be an issue. Secondly, the study recommended that FGC probe biasing be implemented into the plan to optimize the injection of sulphur trioxide and ammonia. Probe biasing is a techniqué whereby each individual injection probe is tailored for the flue gas temperature and gas flows local to that probe. This biasing optimizes the injection of both SO_3 and NH_3 into the flue gas and results in a better resistivity modification and an improved overall system performance.

2.1 Patterned or "Tailored" FGC Injection

The effectiveness of the SO_3 and NH_3 flue gas conditioning is greatly dependent on flue gas temperature and flue gas flow. The current system is setup to treat the worst ash condition and is dependent on boiler load only. This results in over conditioning the flue gas in certain areas and under conditioning in others. By individually tailoring the injection rates for temperature and flow differentials, better sulphur trioxide and ammonia coverage and utilization can be achieved. This results in an overall improvement in the effectiveness of the system and a corresponding improvement in precipitator efficiency. Typically, probe biasing will also result in a reduction in SO_3 and NH_3 consumption due to better utilization.

Ideally, the amount of conditioning gas delivered to any single injection nozzle in the flue gas stream should be proportioned to the amount of ash passing through that nozzle's treatment area and adjusted for the flue gas temperature at that point. It is entirely possible to make comprehensive sets of measurements which determine these values, at least for one set of operating conditions, and it is also possible to divide the delivery of conditioning gas among the injection nozzles in accordance with such measurements. In practice, a full scientific treatment of this type is never done, and is rarely even approximated. The reason, aside from the variability of the target conditions, is that ESP's have a considerable degree of built-in tolerance for random variations. Witness to this fact is provided by many existing installations where FGC was neither needed nor used. It is common in these units to find that a wide spread of temperatures across the air preheater outlets is passed through to the ESP inlet along with non-uniform dust concentrations, in spite of which the ESP exhibits excellent operation.

In general, inlet conditions which meet industry criteria for satisfactory ESP operation, allow treatment of a flue gas conditioning system on the basis of uniform temperature and flow distribution. Another way to state this is that situations which could require special precautions for distribution of conditioning gases usually also require modifications to permit satisfactory ESP operation, and incorporation of the latter will usually eliminate the former.

2.2 Gas Flow Distribution

Another potential upgrade that was identified early in the project definition phase was to review and improve the flue gas flow distribution on the inlet and outlet of the existing precipitator.

In the early 1990's OPG conducted a flow model study on the existing precipitators. As a result of this study, a number of flow correction devices were installed in the existing precipitators. These flow correction devices were for the most part installed on the internal walkways of the precipitator and serve to skew the flow in the precipitator. Skewing the flow in the precipitator is a flow adjustment technique popularized in the early 1990's. This flow correction technique when properly applied is intended to improve precipitator performance. Although installed on the Nanticoke precipitators, the resulting performance improvements were mixed and subjective. Over the years, some of the devices have fallen off or have been removed with little or no consequences to the performance of the precipitators.

As a part of the overall particulate collection improvement program, the project team decided to remove the previous skewed flow devices and install flow correction devices to provide an even gas flow distribution across the inlet and outlet of the precipitators in accordance with industry standards. This technique is the standard for design of new precipitator installations and is documented in the "Institute for Clean Air Companies" guideline "EP-7". The ICAC EP-7 standard is used throughout the industry as the standard for precipitator modeling and when followed, results in a uniform velocity profile at the inlet and outlet of the precipitators.

3 EQUIPMENT

3.1 Boilers

Nanticoke GS has total of eight (8) opposed-fired B&W radiant boilers rated at 490-512 MW gross (3,600,00 lb/hr steam at 2,450 psig) each. Superheat/Reheat temperature is 1,000 °F. Each boiler-unit has 61,300 ft^2 heating surface and 107,700 ft^2 tube transfer surface and is equipped with two Ljungstrom SAH's and one Ljungstrom PAH.

Table 1 presents the recent boiler combustion data based on firing of a blend of up to 80% PRB and up to 20% Eastern Appalachian low sulfur coal

3.2 Fuel Processing and Handling

Each boiler is fired by five (5) B&W 10E Pulverizers with the capacity of:

- 37 tons Eastern Appalachian low sulfur coal or
- 53 Tons when fueling 100 % Powder River Basin (PRB) coal.

Individual pulverizer(s) are feeding particular rows of the burners (A through E).

Table 1. Boiler Combustion Data

Combustion Data (@ 500 MW Gross)	Range	Typical
Stack gas flow rate (am_3/sec)	805 – 900	850
Stack gas temperature (°C)	126 – 150	138
ESP inlet PM loading (g/am_3)	3.1 – 5.0	3.9
ESP inlet fly ash LOI (%)	5.0 – 14.0	9.0
Flue gas conditioning system (in service at all times)		
Current SO_3 injection rate (ppm)		8
Current NH_3 injection rate (ppm)		5

3.2.1 Fuel Characteristics

The units burn a mixture of PRB and Eastern Appalachian low sulphur bituminous coal. The fuel specification below is based on the respective 80/20% PRB/Eastern Appalachian low-sulfur coal blend.

3.2.1.1 Coal Analyses

Table 2 and Table 3 present coal Proximate and Mineral analyses.

Table 2. Coal Proximate Analysis (as received)

Item	Range			Typical
Moisture (%)	14	To	25	23
Volatile matter (%)	30.5	To	34	31
Fixed carbon (%)	39	To	46	40
Ash (%)	5.0	To	8.0	6.0
Sulfur (%)	0.3	To	1.0	0.4
HHV (Btu/lb)	9,300	To	11,000	9,450

Table 3. Coal Ultimate Analysis (as received)

Item	Range			Typical
Carbon (%)	54	To	64	55
Hydrogen (%)	3.6	To	4.3	3.7
Oxygen (%)	8.5	To	12.0	11.5
Nitrogen (%)	0.7	To	1.2	0.9
Sulfur (%)	0.3	To	1.0	0.4
Ash (%)	5.0	To	8.0	6.0
Moisture (%)	14	To	25	23

3.2.1.2 Ash Mineral Analysis

Table 4. Fly Ash Mineral Analyses

Item	Range			Typical
Li_2O (%)				
P_2O_5 (%)	0.7	To	1.8	1.5
SiO_2 (%)	39	To	49	42
Fe_2O_3 (%)	5	To	11	6.5
Al_2O_3 (%)	17	To	24	18
TiO_2 (%)	0.9	To	1.5	1.1
CaO (%)	9	To	18	15
MgO (%)	2.0	To	5.0	4.0
SO_3 (%)				
K_2O (%)	0.5	To	1.3	0.7
Na_2O (%)	0.5	To	1.4	1.0

3.3 Electrostatic Precipitators

Each boiler-unit is equipped with a Joy/Western precipitator (Table 5). Each precipitator has two (2) chambers and three mechanical fields in the direction of the gas flow. The collecting plates are nominally twelve (12) feet long and 30 (thirty) feet tall. Each precipitator is powered by twelve (12) 1,600 mA sets. All T/R sets are equipped with Belco/Merlin AVC's. There are 80 gas passages nine (9) inch wide in each chamber for a total of 160 gas passages across the gas flow.

Original design SCA was 225 ft^2/1000 acfm at a gas flow of 1,538,000 acfm and 246 °F, however, currently the actual gas flow is typically around 1,800,000 acfm and 280 °F, which results in the SCA of about 192 ft^2/1000 acfm.

Table 5. Precipitator Design Data

ITEM	UNITS	VALUE	
		DESIGN	ACTUAL
Design Gas Flow Rate	acfm	1,538,000	1,800,000
Gas Temperature at the ESP Inlet	°F	246	280
Average Gas Velocity	ft/s	7.12	8.4
Specific Collection Area (SCA)	ft^2/1,000 acfm	225	191
Inlet Loading	gr/scf	4.878	2.7
Efficiency	%	99.5	98.5-99.05 (w/FGC)
Treatment Time	s	5.05	4.3
Current Density	mA/ft^2 (plate)	0.0556	0.0556

3.4 FLUE GAS CONDITIONING

3.4.1 FGC Systems

3.4.1.1 SO_3 Flue Gas Conditioning System

The original SO_3 FGC systems were manufactured by Wahlco, Inc. Each FGC system injects SO_3 independently of the ammonia, based on the Boiler Load signal represented by a coal flow rate. The design sulfur flow was rated 0–74 kg/hr as 0-100% on the Ratio Station (controller). Maximum SO_3 flow was 24 ppmV based on flue gas flow of 2,760,870 Nm^3/hr @127 °C and the Ratio Station signal of 100% on use of ¾ in. diameter plunger pump with the pump stroke set to 1 and ⅞ inches. The built-in interlock provides the FGC system shut-off at the fuel flow rate below 20%.

Recently, in the process of the upgrading the old piston-type molten sulfur metering pumps, the latter were replaced with the diaphragm-type LEWA pumps. The deliverable sulfur flow was also reduced by 50%, thus reducing the maximum SO_3 injection rate down to 12 ppmV.

3.4.1.2 NH_3 Flue Gas Conditioning Systems

The NH_3 FGC systems were also manufactured by Wahlco, Inc. Each system was designed to inject NH_3 independently of the SO_3 injection, based on the Boiler Load signal represented by a coal flow rate. The design ammonia flow was rated 0 – 28 kg/hr as 0-100% on the Ratio Station (controller). Maximum NH_3 flow is 20 ppmV based on flue gas flow of 2,760,870 Nm^3/hr @127 °C and the Ratio Station signal of 100%.

3.4.2 Original Injection Probes

3.4.2.1 SO_3 Injection Probes

The SO_3 injection probes are installed downstream of the SAH's in both pant legs of the exhaust gas flow. Initially it was thought to install the SO_3 injection probes in the PAH duct as well, however, due to the lower gas exit temperatures in this duct, it was decided not to inject SO_3 for fear of acid attack in this duct. During initial operation the SO_3 injection probes operated very successfully. However, over time, the probes were prone to pluggage. Consequently, the probes were modified. The latter included "shortening" the probes and adding a single larger nozzle pointing downwards to prevent dust build-up and subsequent plugging. This new SO_3 probe design is the standard at the station.

3.4.2.2 NH_3 Injection Probes

The NH_3 injection probes were installed downstream of the secondary air heaters (SAH) and upstream of the SO_3 injection probes. There were no NH_3 injection probes in the primary air (PAH) duct.

Figure 1. Unit 2 SO_3 Distribution Downstream of the Injection Probes

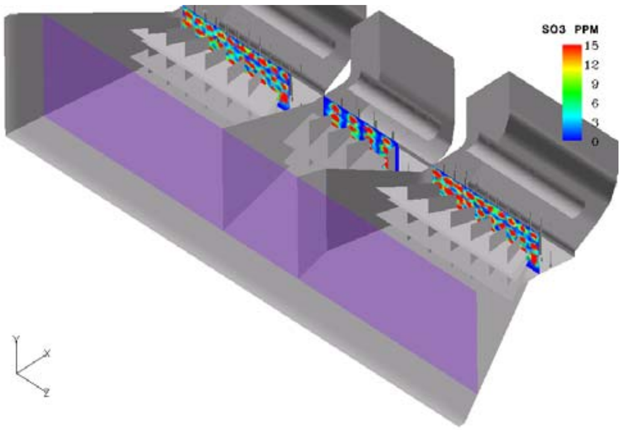

Figure 2. Unit 2 SO_3 Distribution in a Horizontal Plane

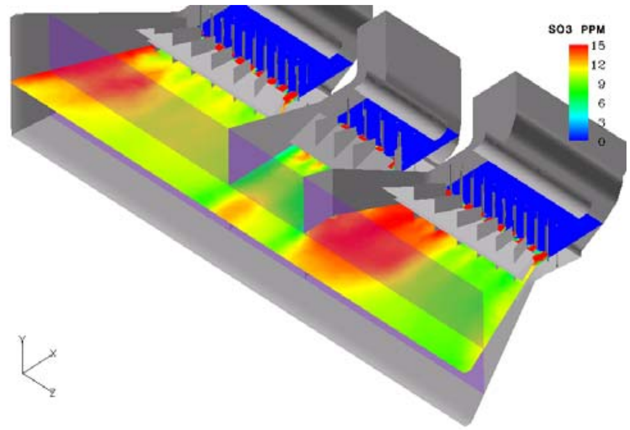

Figure 3. Unit 5 SO_3 Distribution Downstream of the Injection Probes

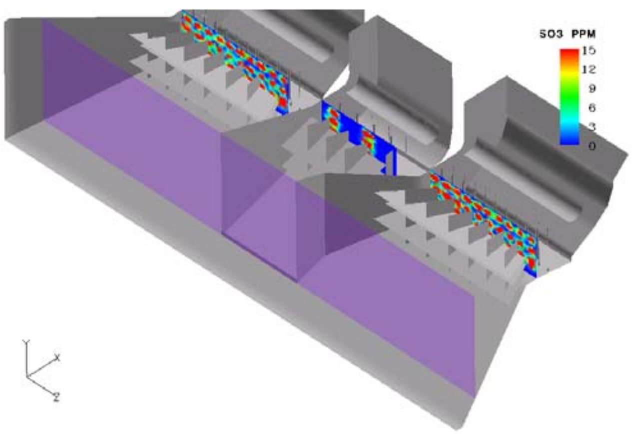

Figure 4.Unit 5 SO_3 Distribution in a Horizontal Plane

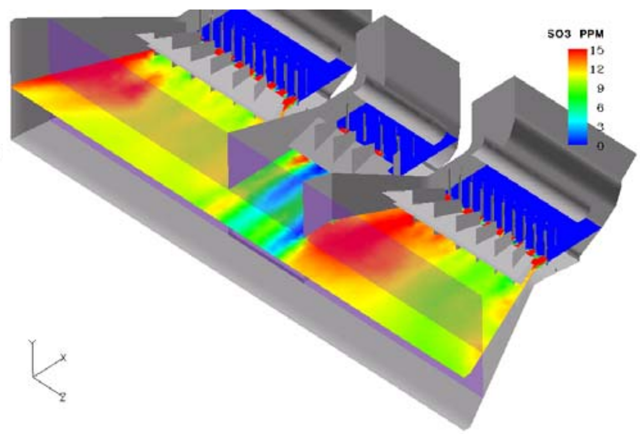

4 WORK PERFORMED

4.1 FLUE GAS CONDITIONING UPGRADES

4.1.1 Design

To determine the number of new SO_3 and NH_3 probes required in the PAH duct and design of the probe biasing, a computational fluid dynamics (CFD) modeling was performed. The CFD included modeling the flue gas flow and temperatures distribution from the air pre-heater's outlet, to the precipitator's inlet. From the CFD model, the proper number of SO_3 and NH_3 probes were determined as well as the optimum injection rates for all the probes to ensure a uniform distribution of SO_3 and NH_3 across the inlet of the ESP.

4.1.2 SO_3 System

Based on the CFD model it was determined that four (4) new SO_3 probes would be required for Unit № 2 and two (2) SO_3 probes would be required for Unit № 5 (Figure 1 and Figure 2). The latter was done in anticipation of a slightly different temperature distribution profile somewhat similar to the one on Unit № 7 due to the new deeper baskets in the Unit № 5 PAH. However, there was a provision made to install an additional two (2) probes on the PAH duct of Unit № 5 if required. As shown on Figure 3 and Figure 4, although there is a provision for the four (4) SO_3 probes, only two (2) are currently being used (shown by the SO_3 flow). The piping design was kept the same for both unit № 2 and № 5.

Table 6. Design Input Data for SO_3 Injection Bias CFD Study

Figure 5. Unit №2 “AS IS” Gas Temperature Distribution

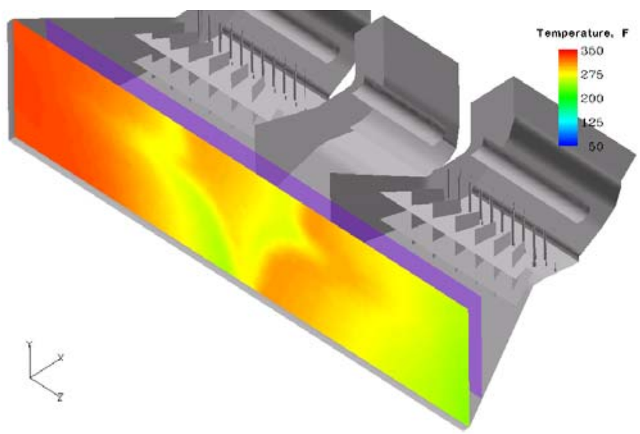

Figure 6. Unit №5 "AS IS" Gas Temperature Distribution

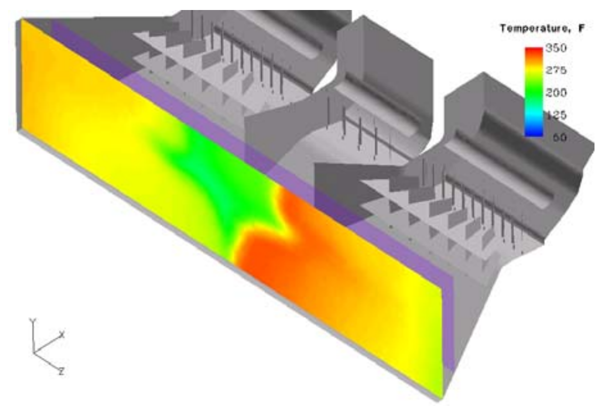

Figure 7. Unit №5 . “Averaged” Flue Gas Temperature Profile

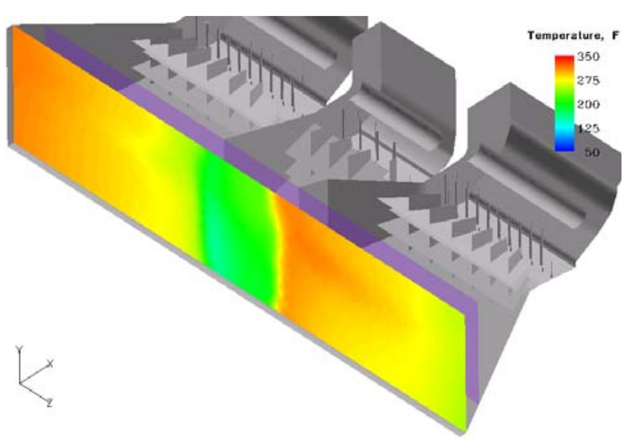

Figure 8. Nanticoke GS Blend SO_3 Theoretical Requirement

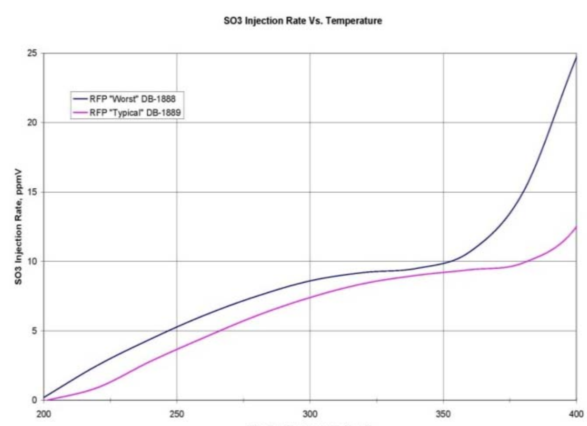

Furthermore, all probes orifices were biased to fine-tune the local injection rates in accordance to the CFD study. As discussed previously, the FGC bias or SO_3 and/or NH_3 injection custom tailoring is typically done to accommodate significant stratification of the temperature or flue gas flow distribution (or both) while providing for a required SO_3 concentration at a selected plane (typically, at a precipitator inlet). For this particular study, Allied Environmental Technologies, Inc. developed a unique approach whereby the SO_3 injection bias was done based on comparing a theoretically estimated SO_3 requirement with CFD computed temperature and SO_3 injection profiles (Table 6). The results of the CFD simulation in the form of specific Correction Coefficients were given to probe supplier (Wahlco, Inc.) who calculated the revised SO_3 flows and re-sized the respective orifices to match the CFD estimates. Subsequently, the CFD model was re-run to corroborate new FGC injection probes operation.

Figure 9 presents a summary of the CFD computed SO_3 Distribution at the Unit №2 ESP inlet. It compares three cases: (a) AS IS without FGC Injection Probes in the PAH duct, (b) with new Injection Probes and "averaged" inlet gas temperature and flow distribution, and (c) results of the SO_3 injection bias based on Wahlco's computed SO_3 flows. Figure 10 presents a summary of the Unit №2 SO_3 "differential" for the above-described three cases. There, Red represents "positive/excess" and the Blue indicates "negative/deficiency" as compared to the theoretically calculated SO_3 requirement at any given point of a selected cross section, in this case, it is projected to the ESP inlet. Clearly, the results confirmed significant improvement in the SO_3 distribution at the ESP inlet plane.

Similarly, Figure 11 presents a summary of the Unit №5 CFD computed SO_3 distribution at the ESP inlet for three cases:

i 4 new SO_3 injection probes (5 NH_3 probes) in the PAH duct; unbiased SO_3 flow,

ii 2 new SO_3 injection probes (3 NH_3 probes), averaged inlet temperature and flow distribution; unbiased SO_3 flow, and

iii Final corroborated bias.

Figure 12 presents a summary of the Unit № 5 SO_3 "differentials" for the above-described three cases.

4.1.2.1 NH_3 System

There were five (5) additional NH_3 injection probes installed in the PAH duct on Unit №2 and three (3) new NH_3 injection probes on Unit №5. New NH_3 probes were of the same design as the current Nanticoke GS design. All ammonia probes orifices were biased to match the revised local SO_3 flows. Similarly to the SO_3 piping, the ammonia piping design was kept the same for Units № 2 and № 5. Accordingly, there was a provision made to install an additional two (2) probes on Unit № 5 if required in the future.

Figure 9. Unit №2 SO_3 Distribution at the ESP Inlet

AS IS – No FGC Probes in the Primary Duct | **With SO_3 Probes in the Primary Duct (Symmetrical Input Data Set)** | **Biased SO_3 Probes**

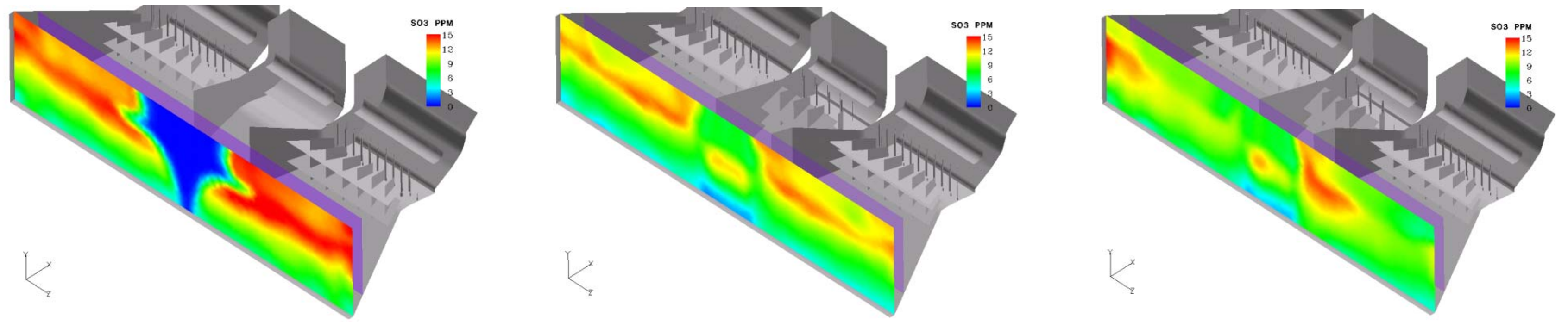

Figure 10. Unit №2 SO_3 Differential Distribution - Difference Between Theoretically Estimated and CFD Computed

AS IS – No FGC Probes in the Primary Duct | **With SO_3 Probes in the Primary Duct (Symmetrical Input Data Set)** | **Biased SO_3 Probes**

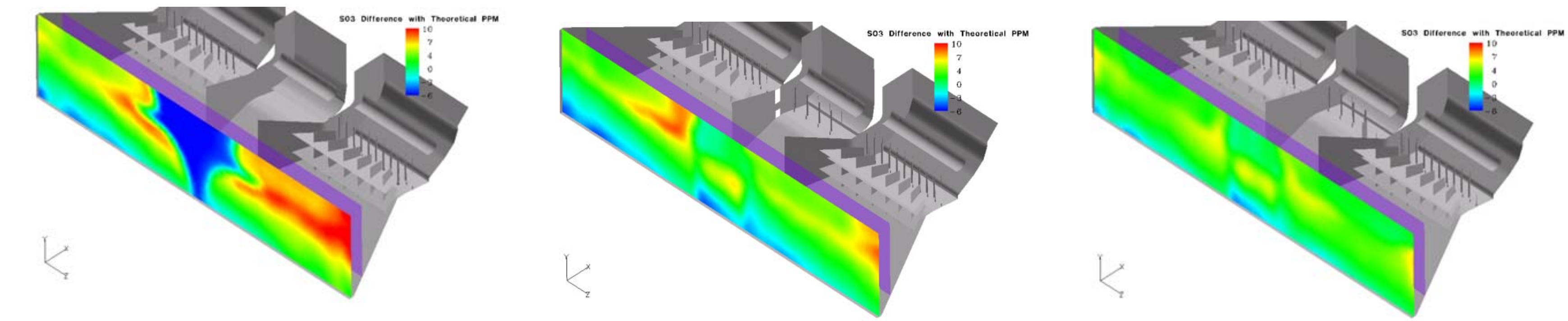

Figure 11. Unit № 5 SO_3 Distribution at the ESP Inlet

4 New SO_3 Probes in the Primary Duct. Unbiased	2 New SO_3 Probes. Symmetrical Input Data Set. Unbiased	Final Bias Review

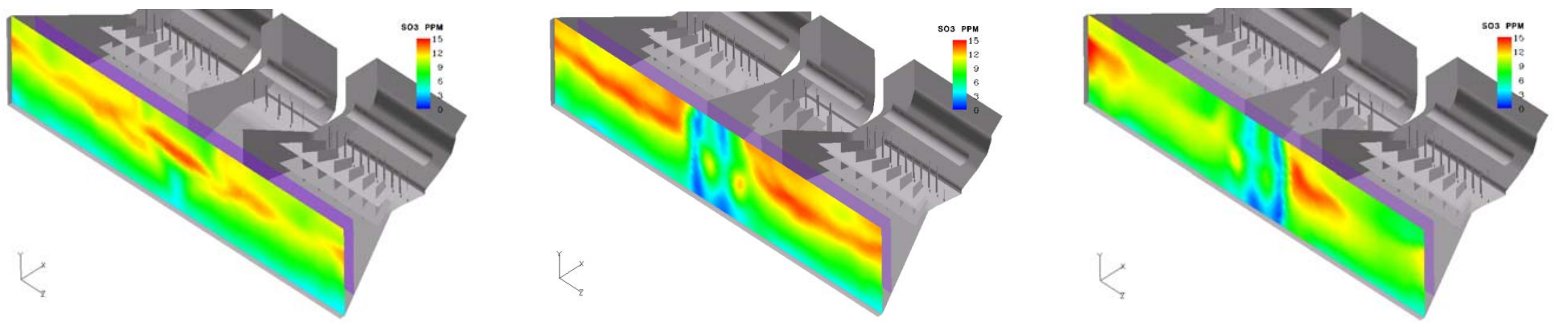

Figure 12. Unit № 5 SO_3 Differential Distribution - Difference Between Theoretically Estimated and CFD Computed

4 New SO_3 Probes in the Primary Duct. Unbiased	2 New SO_3 Probes. Symmetrical Input Data Set. Unbiased	Final Bias Review

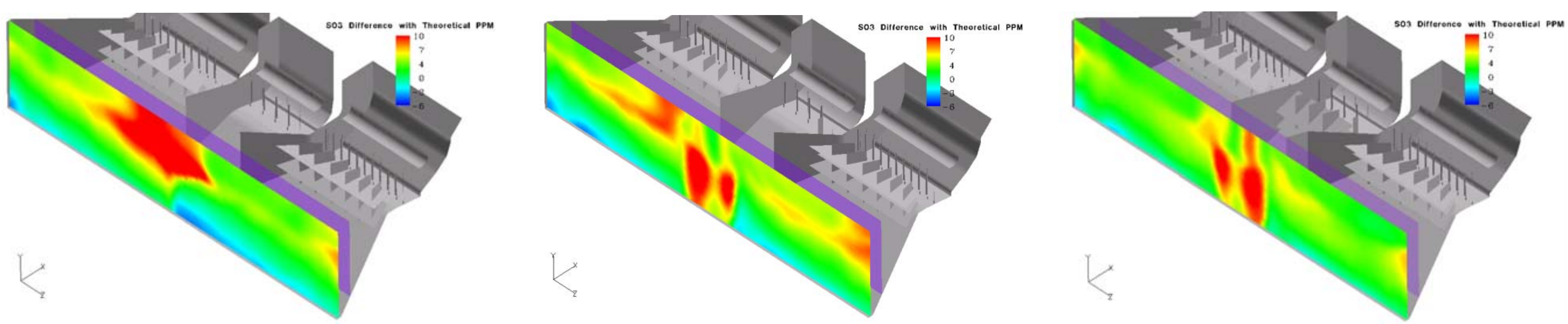

4.2 ELECTROSTATIC PRECIPITATORS

4.2.1 Gas Flow Distribution

Both flow correction techniques (skewed and ICAC) have their proponents and both can provide successful results when properly applied. However, it was decided by the EIP team that a physical model and a CFD model of the precipitator would be constructed and flow devices designed to attempt to achieve the ICAC criteria on the inlet and outlet of the precipitators.

The modeling studies recommend changes to existing flow correction devices or the installation of new flow correction devices in order to achieve the ICAC-EP-7 precipitator inlet and outlet criteria. The physical model suggested that the following items did achieve a precipitator velocity distribution that was acceptable to ICAC recommendations at the outlet of the first and last fields.

(a) Installing a 50% open area vertical strip comb below the existing kicker baffles on the inlet perforated plate.

(b) Removing the skewed flow walkway baffles between the 1st and 2nd, 2nd and 3rd fields.

(c) Removing the existing outlet baffle and installing a 20% open area outlet screen.

The CFD model corroborated the physical model recommendations. Table 7 and Table 8 present a Summary of the gas flow distribution for both Units № 2 and № 5. The flow corrections were performed by installing 20% open screen at the ESP outlet. Visual comparison of the inlet and outlet gas flow distribution on Unit № 2 (Figure 13 - Figure 16 and Figure 14 - Figure 17) confirms significant improvement from the AS IS to ICAC cases. Unit № 5 results also corroborated achieving the ICAC gas flow distribution criteria (Figure 15 and Figure 18) with a 20% open screen at the ESP outlet. Table 8 presents the same summary in a 3-D, while Table 9 demonstrates statistical results calculated at the inlet and outlet of ESP’s for each case-study.

Figure 22 through Figure 24 depict the gas flow distribution along the gas flow from the inlet to the first field to the outlet of the last field. Clearly, adding new 20% open flow correction screen at the precipitator outlet improves the gas flow distribution in both Units № 2 and № 5. Statistical analyses confirmed an agreement with the ICAC EP-7 standards.

From the air preheater outlets to the ID fan inlets the estimated pressure loss measured from the physical model was 0.72” H_2O for a flow of 1,800,000 acfm at 280 °F, an increase of 0.32” H_2O with the new outlet screen added. Table 10 presents a summary of the pressure losses computed by the CFD and measured by the physical model for each case.

Table 7. Precipitators Inlet and Outlet Gas Flow Distribution Summary.

Inlet Gas Flow Distribution

Figure 13. Unit 2 AS IS. "Symmetrical"

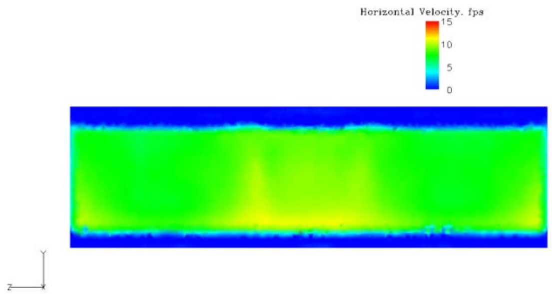

Figure 14. Unit 2 ICAC

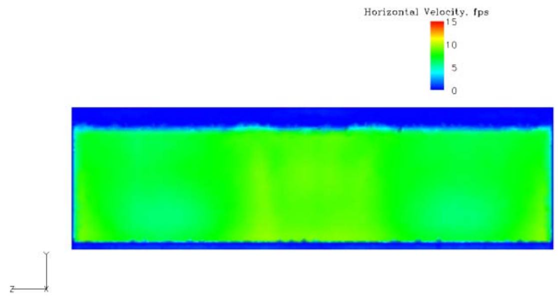

Figure 15. Unit 5 ICAC

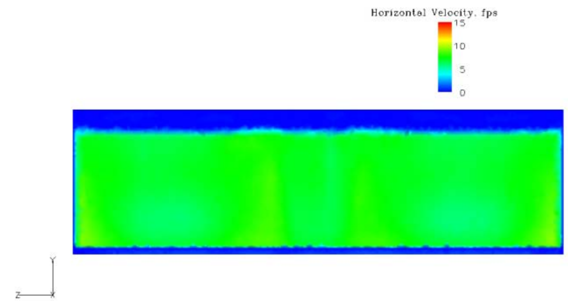

Outlet Gas Flow Distribution

Figure 16. Unit 2 AS IS. "Symmetrical"

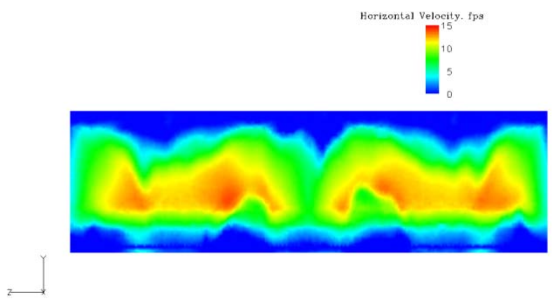

Figure 17. Unit 2 ICAC

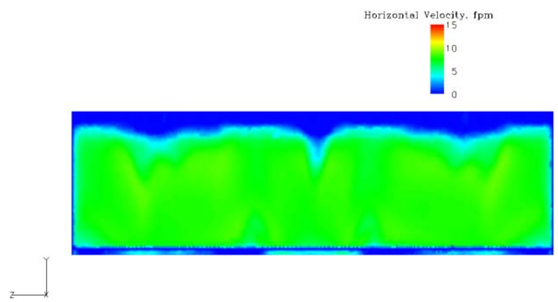

Figure 18. Unit 5 ICAC

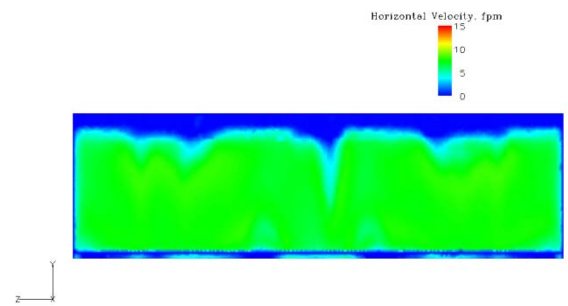

Table 8. Gas Flow Distribution Summary in 3-D

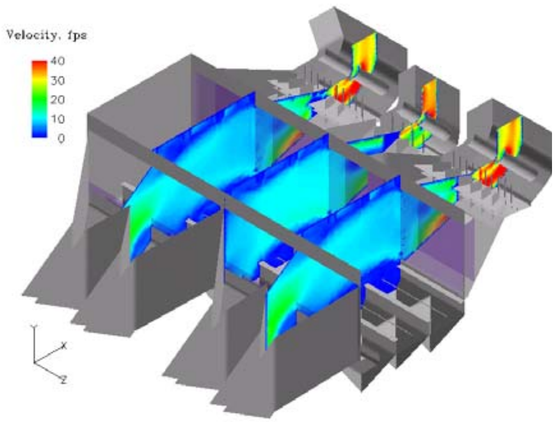

Figure 19. Unit 2 AS IS.

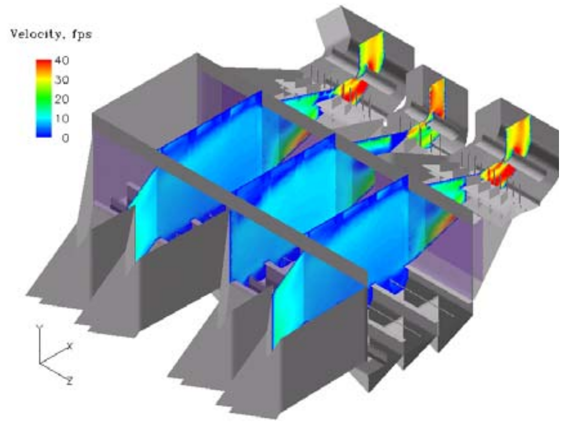

Figure 20. Unit 2 ICAC.

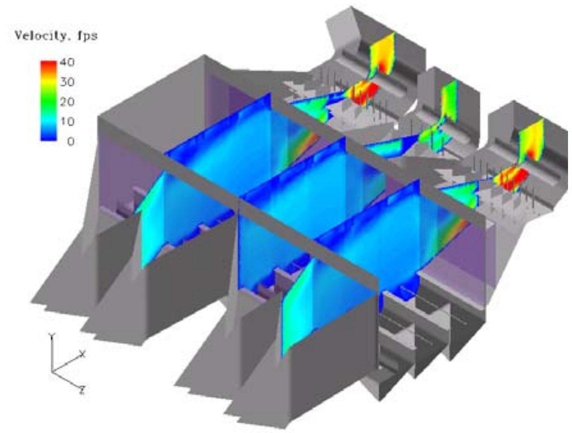

Figure 21. Unit 5 ICAC.

Table 9. CFD and Physical Model Gas Flow Distribution Study Statistics Summary

MOD-EL	CFD												PHYSICAL/COLD FLOW		
Case ID	Unit 2 – AS IS			Unit2 - ICAC			Unit 2 - “Variable” Screen			Unit 5 - ICAC			Unit 2 - ICAC		
Location	Deviation, %		RMS Devia-tion, % of Mean	Deviation, %		RMS De-viation, % of Mean	Deviation, %		RMS De-viation, % of Mean	Deviation, %		RMS De-viation, % of Mean	Deviation, %		RMS De-viation, % of Mean
	1.15 V_{av}	1.4 V_{av}		1.15 V_{av}	1.4 V_{av}		1.15 V_{av}	1.4 V_{av}		1.15 V_{av}	1.4 V_{av}		1.15 V_{av}	1.4 V_{av}	
Inlet	22.2>	0	30.6>	14.9>	0	12.2	15.3>	0	14.4	7.3>	0	10.4	12.8>	0	14.4
Outlet	46.7>	29.1>	65.4>	0	0	5.4	25.8>	0	22.6	9.4>	0	12.6	0.9>	0	8.6

Figure 22. Unit № 2 Gas Flow Distribution – AS IS. Inlet to Outlet (left-to-right).

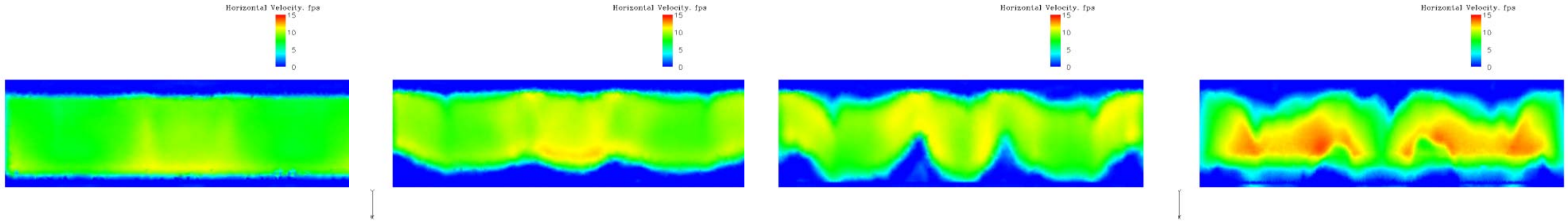

Figure 23. Unit № 2 Gas Flow Distribution - ICAC. Inlet to Outlet (left-to-right).

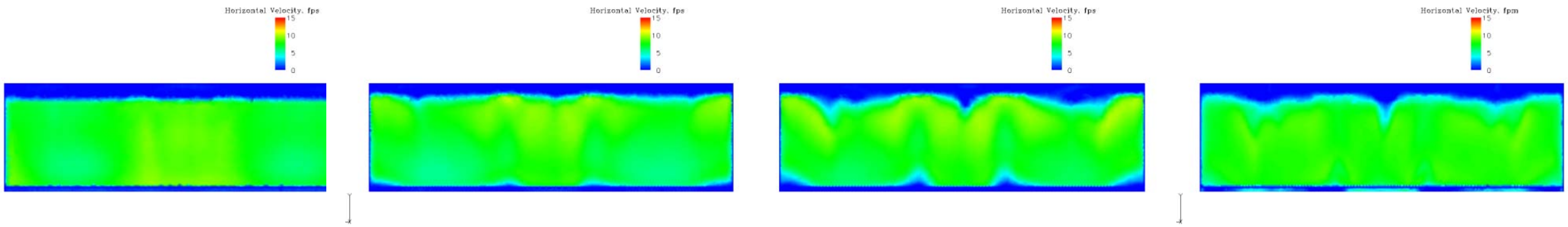

Figure 24. Unit № 5 Gas Flow Distribution - ICAC. Inlet to Outlet (left-to-right).

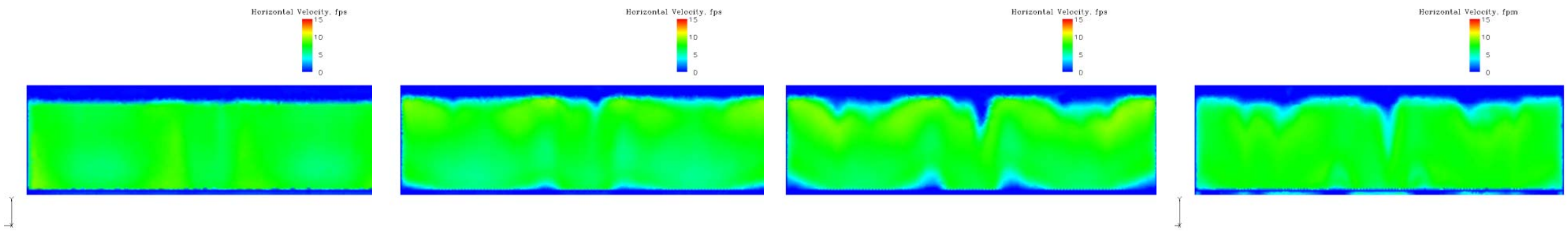

Table 10. CFD and Physical Model Pressure Loss Summary

MODEL	CFD				PHYSICAL/COLD FLOW
Case ID	Unit №2 - ASIS	Unit №2 - ICAC	Unit №2 - "Variable" Screen	Unit №5 - ICAC	Unit №2 - ICAC
Location	Pressure Loss, in H_2O				
Inlet Ductwork	0.31	0.31	0.31	0.29	0.37
ESP	0.11	0.32	0.19	0.31	0.31

5 FGC POST-RETROFIT OPERATION

5.1 UNIT №2

5.1.1 First Trial

The initial FGC injection rates optimization took place during the week of November 13th, 2006. For reasons other that opacity, the unit was limited to the maximum load of about 395 MW. According to the plant information, the coal fired during this period had slightly higher sulfur content.

There were three (3) basic SO_3 with respective NH_3 settings tested (Table 11):

Table 11. First Trail Stoichiometric Ratios Tested

SO_3	NH_3	STOICHIOMETRIC RATIO (SR)
Nominal 54% (6.5 ppmV)	Nominal 21% (4.2 ppmV);	1.55
Nominal 86.5% (10.4 ppmV	Nominal 44% (8.8 ppmV)	1.2
Nominal 42% (5 ppmV)	Nominal 15% (3 ppmV)	1.67

Figure 25 presents relationship between the $\frac{SO_3}{NH_3}$ stoichiometric ratio and the 4-min. average stack opacity at the boiler load in the 389 – 393 MW range.

5.1.2 Second Trial

Second trial took place during the week of March 19th, 2007. During the second trial Unit № 2 was generally operating at the boiler load of about 480-491 MW with the stack 4-min. average opacity in the 7 to 13% range.

On March 20th, 2007 (during the first part of the day), the Unit operated at the boiler load of 400-402 MW, which is somewhat close to the first trial. The 4-min average stack opacity was about 5.8% with SO_3 flow of about 50% and NH_3 flow of 33%. Figure 26 presents the $\frac{SO_3}{NH_3}$ stoichiometric ratio and the 4-min. average stack opacity observed during the first trial with the additional data points from the second trial of the similar boiler load. Although the coal might be slightly different between two trials, the stoichiometric ratio vs. stack opacity appears to be rather similar.

Figure 25. Unit №2 SO_3/NH_3 Stoichiometric Ratio vs. Opacity – First Trial @ 389-398 MW

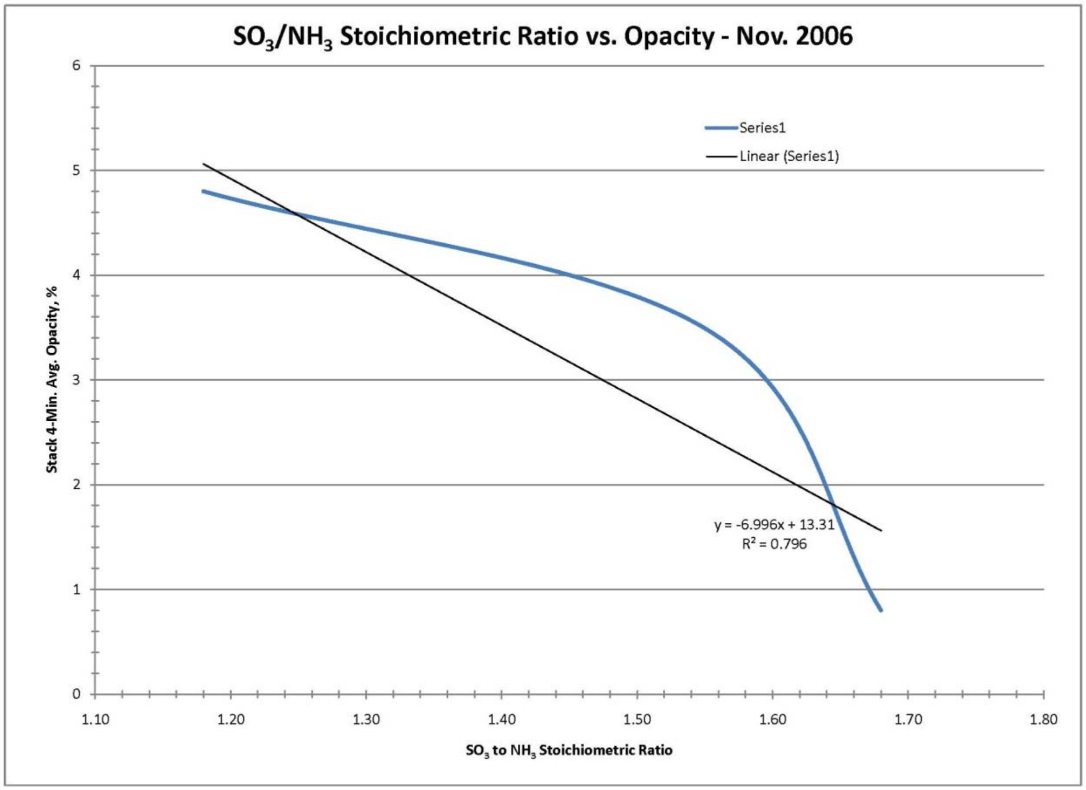

Figure 26. Unit 2 SO_3/NH_3 Stoichiometric Ratio vs. Opacity @ 389-398 MW

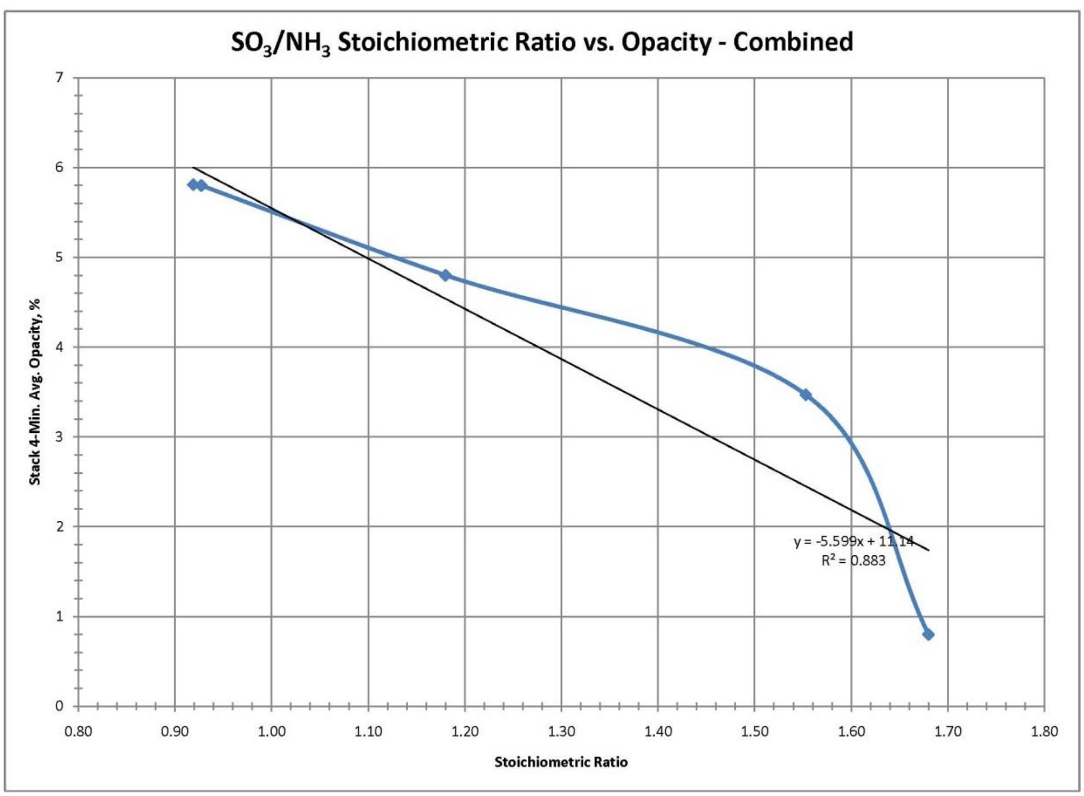

Following days were devoted to a "Trial and Error" type search for the optimum $\frac{SO_3}{NH_3}$ stoichiometric ratio with respect to the lowest 4-min stack avg. opacity. As it turned out, the "old" ratio of 70% (8.4 ppm) SO_3 to 30% (6 ppm) NH_3, which corresponds to the $\frac{SO_3}{NH_3}$ stoichiometric ratio of about 1.4 seems to be most agreeable with overall boiler load range for Unit № 2.

5.2 UNIT №5

The Unit № 5 optimization was conducted during the week of March 19th, 2007. The unit was operated at the maximum load with the 4-min. stack average opacity in the range of 8-10% with the SO_3 injection rate of 52% (6.25 ppm) and ammonia flow in the range of about 30% (6 ppm). The latter corresponds to the $\frac{SO_3}{NH_3}$ stoichiometric ratio of about 1.04.

Rather that investigating further, it was recommended to stay with the same injection rates combination as on Unit № 2, i.e. 70% on the SO_3 flow and 30% on ammonia.

6 RESULTS

Based on the comparison of the operating data, it was observed that the performance of Nanticoke Unit № 2 precipitator significantly improved following the modifications performed (Figure 27). Improvements observed are the following:

Figure 27 Unit № 2 Performance Summary

Delta of 65 MW

		After	Before							
Date		Jan. 8, 2007	Mar. 29, 2006		Jan. 8, 2007			Mar. 29, 2006		
Start Time		13:45	8:47		13:45			8:47		
End Time		18:26	17:40		18:26			17:40		
Coal Blend		A,B,C,D-PRB, E-USLS								
	Unit	Average	Average	Difference	STDEV	Maximum	Minimum	STDEV	Maximum	Minimum
Load	MW	484.5	419.7	64.8	5.1	490.3	468.3	4.3	429.3	400.7
4-min Opacity	%	10.4	10.6	-0.2	0.6	12.2	9.2	2.5	19.8	6.4
Coal Flow	kg/s	63.8	55.0	8.9	0.6	65.1	61.7	1.1	59.3	50.9
Instant. Opacity	%	10.4	10.7	-0.3	0.8	14.3	8.8	3.3	40.1	5.9
Flue Gas Temp.	deg.c	161.6	164.8	-3.2	0.6	163.2	160.8	0.8	167.2	162.3
Total Air Flow	kg/s	536.6	456.2	80.5	7.3	546.6	515.3	7.8	477.4	423.7
Total Power	kW	534.5	374.5	160.0	21.6	577	471	20.6	435	322
SO3	%	40.9	42.1	-1.2	2.6	49	40	0.5	44	41
NH3	%	14.6	0.0	14.6	0.9	17	14	0.0	0	0
A1A	kW	25.2	17.3	7.9	1.5	29	22	1.7	20	12
A1B	kW	38.3	13.9	24.4	3.5	47	32	1.0	16	8
A2A	kW	25.9	10.3	15.6	0.9	28	24	0.9	13	7
A2B	kW	29.1	26.3	2.8	5.4	44	22	6.7	38	13
B1A	kW	65.2	41.4	23.8	7.5	70	33	6.3	61	30
B1B	kW	56.2	22.4	33.8	3.3	58	34	1.7	29	14
B2A	kW	50.0	13.6	36.4	12.0	70	31	1.0	17	11
B2B	kW	54.9	37.4	17.5	2.4	57	36	4.5	60	30
C1A	kW	49.1	54.8	-5.7	0.5	51	48	8.7	64	28
C1B	kW	46.2	22.5	23.7	0.6	47	45	16.2	63	8
C2A	kW	45.9	54.8	-8.9	0.4	47	45	9.3	71	36
C2B	kW	48.3	59.6	-11.4	0.5	49	46	0.5	60	58
A Row	kW	118.6	67.9	50.7						
B Row	kW	226.4	114.8	111.6						
C Row	kW	189.5	191.8	-2.3						

Decrease in Opacity Range

1. Average Opacity improvement – reduction 2-3%;
   (i) When operating at a load of 50 MW greater than prior to the modifications, opacity did not deteriorate – opacity maintained same overall average.
   (ii) Opacity reduction in the high load range under similar comparison conditions.

2. Reduced level of Opacity spikes;

   (i) Opacity excursions have been sizably reduced. The opacity values, both for the 4-min and instantaneous, do not vary to the same magnitude following the outage.

   (ii) Magnitude of opacity (%) spikes observed has sizably decreased.

   (iii) The general trend of improved opacity stability, with less variation, is consistent across multiple comparison scenarios.

3. ESP Power consumption has improved

   (i) Improvement observed, particularly on rows A and B.

7 SUMMARY

Nanticoke GS identified a number of key projects that would help the station accomplish this goal. During 2006 – 2007 time period several projects where implemented on Units №2 and №5:

(i) Design and installation of the additional FGC injection probes in the PAH's of both units,

(ii) SO_3 and NH_3 injection probes bias to tailor to the current flue gas temperature and gas flow distribution patterns, and

(iii) Conversion of the ESP's gas flow distribution from the "skewed" flow distribution concept to the "uniform" as described in the ICAC EP-7 document.

Thus far, both Unit №2 and №5 demonstrated significantly reduced stack opacity confirming the ESP's overall performance improvement. The station has decided to replicate this work scope on Units 1, 3, and 4.

7.1 Unit № 2

The first trial was conducted in November 2006. For reasons other than opacity, the Unit № 2 load was limited to about 380-395 MW. Several combinations of the SO_3 and NH_3 flows were tested with the 4-min. avg. stack opacity approaching 1%. The second trial took place in March 2007 with the Unit № 2 boiler load around 495 MW. The 4-min. avg. stack opacity this time was in the range of 10-13%.

The comparisons under different scenarios show apparent improvements, in terms of the opacity level and the magnitude of opacity excursion, as a result of the various modifications. The reduction in either the average (4 minute) or instantaneous opacity will help to alleviate the operational problems associated with the unit being limited by opacity.

The benefits of individual modifications performed on the ESP, such as the addition of FGC injection points at the PAH duct, cannot be ascertained from the above assessment. This could only be made by special arrangement, for example, shutting off the FGC to the PAH duct.

Quantitative assessment on the overall improvement in ESP performance on Unit №2 will be made at the time of the particulate sampling test.

7.2 Unit № 5

The Unit 5 trial was conducted during the week of March 19, 2007. The boiler load reached 520 MW with the 4-min stack avg. opacity of about 8 – 10%.

Based on the up to date data available, the "old" ratio of 70% (8.4 ppm) SO_3 to 30% (6 ppm) NH_3, which corresponds to the $\frac{SO_3}{NH_3}$ stoichiometric ratio of about 1.4 seems to be most agreeable with overall boiler load range and coal supply/blends variations for both Units №2 and №5.

Contact information:

[i] Mr. Thomas L. Lumley, Business Programming Manager, Nanticoke GS +1 (519) 587-2201 x3478

[ii] Mr. Marc D. Voisine P. Eng, Project Engineering Manager, Neill & Gunter +1 (506) 451-1214

[iii] Dr. Henry V. Krigmont, QEP, Allied Environmental Technologies, Inc. +1 (714) 799-9895